Surface faulting of the 26 December 2018, M_w5 earthquake at Mt. Etna volcano (Italy): geological source model and implications for the seismic potential of the Fiandaca fault

R. Azzaro[1], S. Pucci[2], F. Villani[2], R. Civico[2], S. Branca[1], M. Cantarero[1], E. De Beni[1], P.M. De Martini[2], F. R. Cinti[2], M. Caciagli[3], L. Cucci[2] and D. Pantosti[2]

[1]Istituto Nazionale di Geofisica e Vulcanologia, Piazza Roma 2, 95123 Catania, Italy.

[2]Istituto Nazionale di Geofisica e Vulcanologia, Via di Vigna Murata 605, 00143 Roma, Italy.

[3]Istituto Nazionale di Geofisica e Vulcanologia, Via Donato Creti 12, 40128 Bologna, Italy.

Corresponding author: Raffaele Azzaro (raffaele.azzaro@ingv.it)

Key Points:

- The pattern of the 2018 rupture is characterised by scale-invariant overlapping systems of structures organised in a hierarchical way
- The along-strike distribution of the coseismic vertical displacement mimics the pattern of the long-term morphological throw of the fault
- Findings constrain fault behaviour and uniform slip model as a possible input for fault-based seismic hazard assessment

Abstract

At Mt Etna (Italy), volcano-tectonic earthquakes produce impressive surface faulting despite their moderate magnitude (M<5.5), with historically well-documented ruptures featuring end-to-end lengths up to 6-7 km. The 26 December 2018, M_w 5.0 earthquake represents the strongest event of the last 70 years, with ground ruptures extending for ~8 km along the Fiandaca fault, a partially

hidden structure in the volcano's eastern flank. Field data collected by the EMERGEO Working Group (INGV) are integrated in this work with high-resolution photogrammetric surveys by drone, and then interpreted to shed light on the faulting mechanism of the 2018 earthquake as well as on the morphotectonic process of fault growth. The deformation zone shows a complex pattern, characterised by structures arranged in *en-échelon* scale-invariant overlapping systems. Offsets and kinematics vary along the strike due to the fault bending, with a prevailing right-lateral displacement in the northern section and a dextral oblique slip in the southern one (max 35 cm); the dip-slip component increases southward (max 50 cm) and mimics the pattern of the long-term morphological throw of the fault. The kinematic analysis indicates a quasi-rigid behaviour of the two crustal fault blocks and suggests a geological model of rupture propagation that explains the location of the seismic asperity in the northern section of the Fiandaca fault, and the unclamping in the southern one. These findings are used to constrain a conceptual model of the fault in terms of behaviour, representing insights for fault-based seismic hazard assessment.

1 Introduction

On 26 December 2018 (02:19 UTC), a M_w 5.0 earthquake [revised magnitude from CPTI15 catalogue, see *Rovida et al*., 2021] struck Mt. Etna (Italy), the large polygenetic basaltic volcano formed about 500 ka at the outer edge of the Apennine-Maghrebian thrust-belt in Sicily (Figure 1a) [*Lentini et al.*, 2006]. While at first glance the continuous volcanic activity might appear the major threat for the striking strombolian explosions from the summit craters or for the lava flows discharged from eruptive fissures, it is in fact the so-called volcano-tectonic seismicity that represents a significant source of hazard for local communities living on the densely urbanised flanks of the volcano, frequently exposed to the shaking of shallow but small-size earthquakes ($M < 5$, $h < 4$ km) [*Azzaro et al.*, 2017]. It is commonly accepted that the local tectonic activity is the result of the interaction among regional tectonic stress, volcano dynamics (inflation due to magma uprising, dyke intrusions) and flank instability processes [*Azzaro et al.*, 2013a; *Ruch et al.*, 2013; *Urlaub et al.*, 2018, and references therein]. On the other hand, field evidence of surface faulting is widespread along Mt. Etna's active tectonic structures, with even impressive coseismic displacements in some circumstances (vertical offsets up to 90 cm, strike-slip up to 50 cm) [*Azzaro*, 2004; *Acocella and Neri*, 2005; *Barreca et al.*, 2013].

The seismological background of the 26 December 2018, M_w 5 mainshock can be ascribed to the intense seismic swarm accompanying the 24 December 2018 eruption, when a 2 km-long fracture opened on the southern flank of the summit craters (Figure 1b) [*Alparone et al.*, 2019; *Bonforte et al.*, 2019]. Initially, earthquakes mostly affected the upper part of the volcano, but from 26 December seismicity migrated toward more peripheral sectors, culminating with a M_W 5.0 event at 02:19 UTC of the same day. This earthquake, located at a depth of less than 1 km [*Alparone et al.*, 2019], caused heavy damage in the area between the villages of S. Maria la Stella and Fleri (Figure 1b), with more than 1100 left homeless, though fortunately without any victims [*QUEST Working Group*, 2019]; besides seismic shaking, remarkable effects were produced by the pervasive surface faulting along the Fiandaca fault, a semi-hidden structure of the Timpe tectonic system [*Civico et al.*, 2019; *Villani et al.*, 2020; *Romagnoli et al.*, 2021; *Tortorici et al.*, 2021]. The seismic activity along this fault continued until mid-February 2019 with some 50 small aftershocks, one of which reached M_L3 [*Alparone et al.*, 2019].

The 26 December 2018 earthquake occurred in a sector hit by most of the past destructive earthquakes (Figure 1c). The high seismic hazard of the eastern flank of Etna is closely related to the activity of the Timpe tectonic system whose recurrent seismic history, well-known since the 1800s, is characterised by earthquakes very similar to the 2018 event, both in terms of magnitude and effects produced (extent of surface faulting), occurring with mean recurrence times of ~25 years [*Azzaro et al.*, 2013b]. Overall, the seismogenic activity of these faults is not always directly linked to the eruptive activity of Etna, and only in some circumstances can the influence of stress change due to dyke intrusion in triggering fault slip be assessed, as in the case of the 2018 eruption-earthquake [*De Novellis et al.*, 2019].

With a rupture length of ~7.5 km [*Civico et al.*, 2019] and displacements up to 50 cm in throw and 35 cm in strike (right-lateral), together with relevant extensional components (30-45 cm in heave) [*Villani et al.*, 2020], the M_w 5.0 2018 earthquake represents the most significant event in terms of extent and complexity of the surface rupture observed in the Etna region during the past 70 years. This event activated the EMERGEO Working Group – the INGV team devoted to the prompt survey of the geological effects of earthquakes at the surface [https://www.ingv.it/emergeo/] – to undertake a detailed mapping before field evidence could be modified or concealed by weathering or man-made interventions. As a result, for the first time at Etna, the field campaign produced a high-resolution mapping of the coseismic ruptures [mapping

scale up to 1:500, *Civico et al.*, 2019], a photographic collection of the associated geomorphic features [*Cucci et al.*, 2019] and a georeferenced surface slip dataset consisting of more than 900 georeferenced records [*Villani et al.*, 2020].

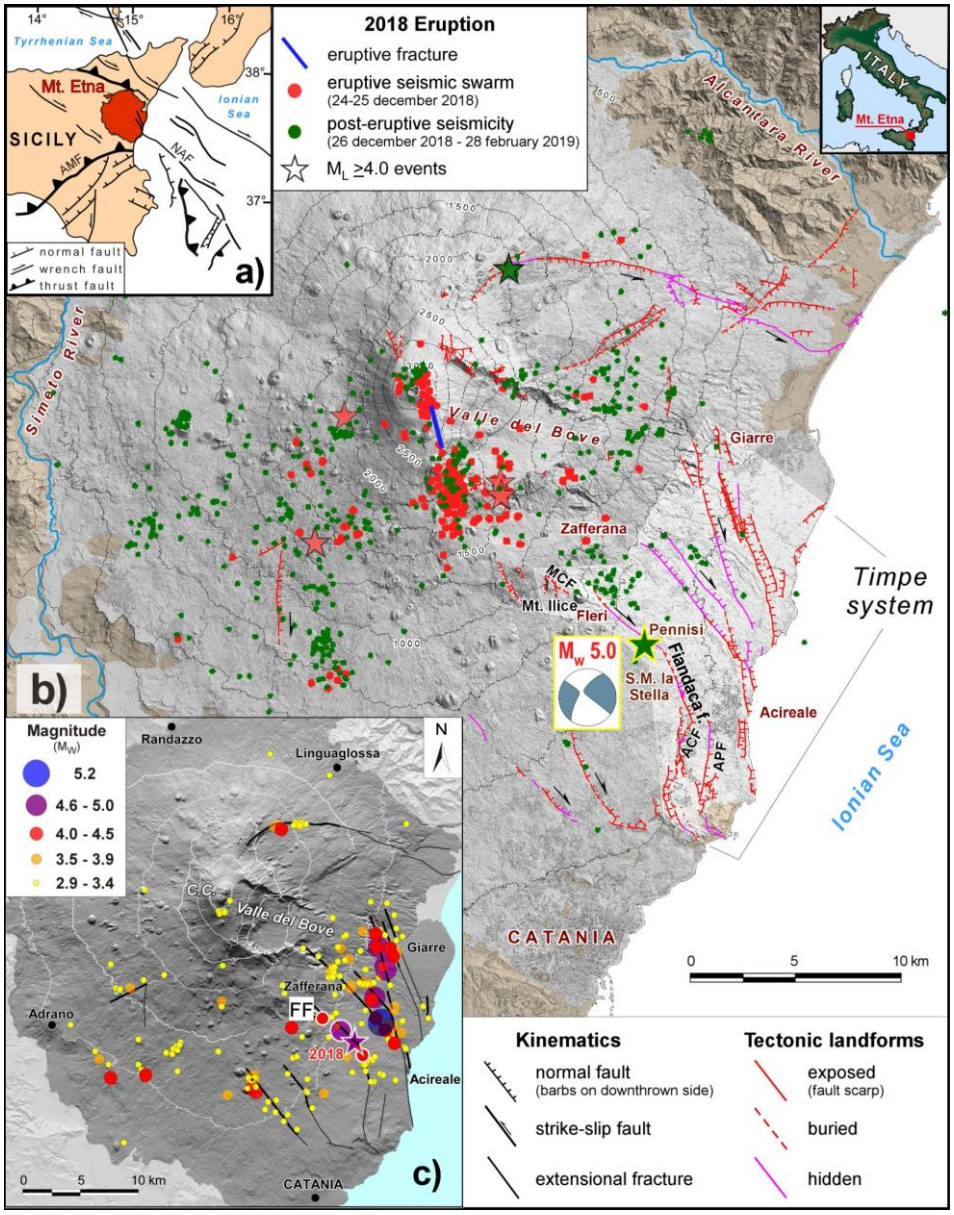

Figure 1. (a) Sketch map illustrating the location of Mt. Etna volcano within the regional structural setting of Eastern Sicily: AMF, Apennine-Maghrebian front; NAF, north Alfeo fault. (b) Distribution of the seismicity related to the 2018 eruption [data from *Alparone et al.*, 2019] in the volcano-tectonic framework described in the text [modified from *Azzaro et al.*, 2012]: ACF, Aci Catena fault; APF, Aci Platani fault; MCF, Monte Cicirello fault. The epicenter of the M_w 5.0 earthquake is marked by a green star; the focal mechanism is from Regional Centroid-Moment Tensors [http://rcmt2.bo.ingv.it/]. (c) Main historical earthquakes from 1633 to 2018 [data from *CMTE Working Group*, 2019]; the events associated with the Fiandaca fault (FF) are bolded in white; C.C. indicates the summit central craters.

In this paper, we exploit data collected in the field with the aim of shedding light on the surface faulting process in a complex volcanic environment such as Etna, that could help in understanding the relationship between the faults slip and the volcano dynamics [e.g. *Azzaro et al., 2013a*; *Solaro et al.*, 2010; *Bonforte et al.*, 2011; *Monaco et al.*, 2021]. Through the detailed analysis of the field measurements, flanked by drone images for some key-areas, we recognise different geometries and kinematic features of the surface faulting along the strike, highlighting the complexity of the deformation zone at a local scale. Moreover, we robustly identify the trace of the Fiandaca fault, and relate the 2018 earthquake rupture with the long-term process of fault growth. Finally, we interpret the 2018 earthquake rupture within the framework of the seismic history of this fault, providing further constraints on its behaviour, segmentation and seismogenic potential, which would improve recent fault-based seismic hazard assessment of the Mt. Etna region [*Azzaro et al.*, 2017].

The case-study of the M_w 5.0 2018 earthquake also represents a possible contribution of field geologists for territorial planning, especially in terms of site-specific fault displacement hazard analyses [e.g. *Baize et al.*, 2019], in a region where surface faulting, either due to fast coseismic slip or to creep, has a perfect natural lab.

2 The Fiandaca fault: seismotectonic and geological background

The Fiandaca fault (hereinafter FF) is the southernmost element of the Timpe tectonic system that, with a series of parallel east-facing step-faults, represents the main tectonic structure dissecting Mt. Etna's eastern flank [*Azzaro et al.*, 2017]. Like other faults of the Timpe system, the behaviour of the FF appears to be governed by two rupture mechanisms, creep along the southernmost section of the fault and earthquake-related slip along the central and northern sectors (Figure 2a), linked by a transition zone characterized by a dual behaviour [*Azzaro*, 2004; *Azzaro et al.*, 2020]. The tectonic activity of the FF is characterized by slip-rates varying considerably in space and time, with long-term values obtained by geological means ranging from 2 to 3.6 mm/yr along the southern stable-sliding segment (ACF section in Figure 1b), punctuated by creep pulses up to 6 mm/yr on shorter time-spans (measured by means of GNSS and conventional geodetic monitoring of man-made features). These short-term slip rates drop to 1-2 mm/yr on the central-northern section of the fault, as expected along locked segments (i.e. seismogenic) [*Azzaro et al.*, 2012]. However, it can be difficult to obtain comparable estimates between geological or geodetic

128 slip-rates in a highly variable tectonic loading environment, driven by the volcano dynamics.
129 Moreover, the role of the erosive or constructive processes (i.e. lava-flows hiding faults), as well
130 as the uncertainty in geochronology dating, may be high on longer time scales.

131 Since the mid-1800s, the seismic history of the FF has been marked by a long list of
132 historical earthquakes causing surface ruptures that affected different patches of the fault
133 according to the scheme in Figure 2b: a number of events have ruptured short sections along the
134 central-southern part of the fault, while the northern section has mostly been affected by longer
135 ruptures, as in the case of the 1894 and 2018 earthquakes. Note also the rupture sequence (as for
136 other faults of the Timpe tectonic system) of the two successive events that occurred during 1984.
137 In general, it has been observed that the historical ruptures maintain the same kinematics along the
138 same fault segments and the offsets depend approximately on the magnitude of the earthquakes
139 [*Azzaro*, 1999]. As for the FF, historical data indicate two main rupture mechanisms: (i)
140 extensional displacements with a minor right-lateral component along the N-S trending section of
141 the fault; (ii) prevailing dextral, oblique slip along the NW-SE trending segment; the maximum
142 dip-slip and right-lateral components of the historical displacements are in the order of 20 and 15
143 cm, respectively.

144 The 1894 (M_w 4.8, value converted from macroseismic intensity according to the
145 relationship by Azzaro et al., 2011) and 2018 (M_w 5.0, value instrumentally determined)
146 earthquakes appear as the major events having entirely ruptured the FF (Figure 2b). The lithology
147 crossed by the FF strongly controls the morphology as well as the surface expression of the 2018
148 earthquake rupture. In fact, the oldest lava flows of the study area, well-exposed along the Aci
149 Catena fault section (labelled as ACF in Figure 1b), form an east-dipping tectonic scarp (Timpe
150 phase and Ellittico volcano in Figure 3). Conversely, north of the Aci Catena village, the fault trace
151 is entirely covered by the recent lava flows and pyroclastic successions of the Mongibello volcano,
152 which erupted in the past 15 kyr (Figure 3). These products derive from the flank eruptions that
153 occurred in prehistoric and historic epochs [for details see *Branca et al., 2011a,b*; *Branca and*
154 *Abate, 2019*]. In particular, the FF fault trace between the villages of S. Maria la Stella and Fleri
155 is hidden by wide lava fields formed in the Roman epoch during the flank eruptions of Mt. Salto
156 del Cane, dated 150 ± 200 BCE, and in the Middle Ages with the extensive lava flows generated
157 by the Mt. Ilice and Mt. Rosso scoria cones, dated 1030 ± 40 CE and 1329 CE, respectively
158 [*Tanguy et al., 2012; Branca and Abate, 2019*].

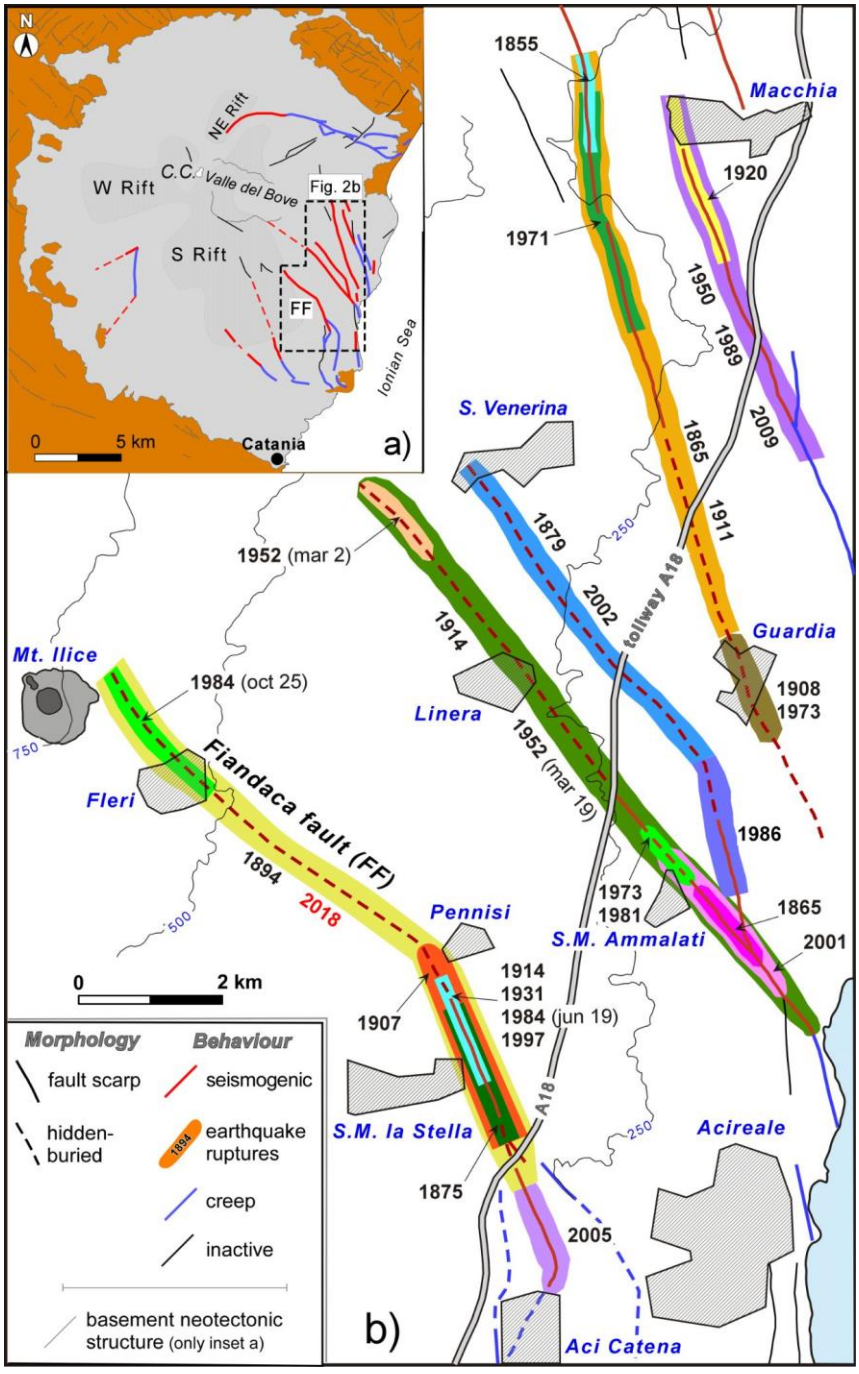

Figure 2. (a) Seismotectonic model of the Etna region showing the active faults and their behaviour. In brown, the sedimentary and metamorphic basement underlying the volcano. (b) Patterns of the historical earthquake ruptures along the Timpe tectonic system [modified from *Azzaro* et al., 2017]; colors indicate different faulting episodes (years in bold). Note that major ruptures affecting the whole fault length have longer recurrence times than the individual patches (i.e. ruptures associated with minor earthquakes).

The morphology of the FF is characterised by a marked arcuate pattern trending broadly N-S to the south. Here, it shows multiple fault strands and a fault scarp height of maximum ~80 m along the ACF (Figure 1b). Moving northwards, the fault trace morphology gradually disappears, being buried beneath the above-described Mongibello lava flows. Near the village of S. Maria la Stella, it is still expressed by a straight NE-facing smoothed scarp, striking N340° and ~10 m high, while the morphological evidence definitively vanishes on approaching the village of Pennisi. Uphill, the continuation of the FF becomes a hidden feature [sensu *Yeats et al.*,1997], i.e. the fault trace is not indicated by a clear and permanent morphology but is revealed only by short-lived ground ruptures and scarplets caused by earthquakes occurring in the past few centuries. The northernmost section of the fault, mapped by *Azzaro et al.* [2012] before the 2018 event exclusively on the basis of the description of past earthquake ruptures [see *Azzaro,* 1999], appears to rotate along a bearing of N320° and to terminate at the base of the pyroclastic cone of Mt. Ilice (Figure 3).

3 Features of earthquake faulting

3.1 Fault mapping

The effects of surface faulting produced by the 26 December 2018 earthquake immediately appeared impressive for the extent of the rupture, amount of displacement and complexity of the deformation zone, even when compared to the major historical events known in the area [*Azzaro*, 1999]. For this reason, we carried out a systematic field survey with the aim of documenting in detail any geomorphic and structural elements related to the fault slip on both natural and human environments. Following the classical morphotectonic and structural geology methods and supported by modern technological tools – digital mobile devices equipped with a specific software and GPS, flanked by drone aerial photos – we collected data on the position, orientation and offset of newly-formed ground ruptures and fault scarplets on soils, consolidated or loose volcanic deposits and massive lavas, as well as fractures and dislocations affecting man-made features (e.g. buildings, roads, fences, etc.) [details in *Civico et al.*, 2019].

While the main goal was to reconstruct the type and scheme of the coseismic deformation as a whole, much effort was required to guarantee a dense sampling of the coseismic effects – nearly 10 m-spaced observation points, on average – in a very urbanized area with limited access to private properties; this substantial work produced a huge dataset of 932 field measurements [see

196 *Villani et al.*, 2020]. Moreover, since the coseismic rupture also affected the hidden section of the
197 FF, it was particularly important to distinguish primary faulting effects from secondary ground
198 fracturing; in this way, we mapped with precision the fault pattern in a sector previously lacking
199 details of the tectonic structure.

200 Figure 3a shows the overall pattern of the 2018 fracture system, simplified from local
201 details as mapped in *Civico et al.* [*2019*]. The fault rupture extends for a length of ~8 km along the
202 FF and can be divided into two sections characterised by different features. The southern section,
203 between Aci Catena and Fiandaca, develops at the base of the NNW-SSE trending fault scarp,
204 exhibiting dip-slip movements associated with a significant tensional component producing
205 prominent open-mode fractures. Approaching the village of Pennisi, the rupture appears as a
206 complex shear system with significant strike-slip components that, after a rotation in the NW-SE
207 direction, extends up to the village of Fleri, terminating on the eastern flank of Mt. Ilice. Finally,
208 some off-fault ruptures have been documented eastwards, in the vicinity of Aci Catena and along
209 the splay fault branching out from the FF (labelled as APF in Figure 1b). These ruptures can be
210 interpreted as secondary ground displacements triggered by the 2018 earthquake along fault
211 sections connected to FF and also known to be prone to creep effects [*Rasà et al.*, 1996].

212 Four target-areas (Figure 3a) were also surveyed by means of a DJI Phantom 4 Pro drone,
213 operating in automatic mode with a fly altitude ranging between 30 and 60 m above ground level.
214 Images were acquired by a 20 Mpx camera and then elaborated by Structure-from-Motion
215 techniques to create orthophotos and DEMs with an average resolution of 1 cm/px [SfM
216 photogrammetry, see *Westoby et al., 2012*]. Relevant details of slip complexities in these areas are
217 discussed in the following paragraph. We recognised different geometries of the coseismic
218 features. Ground ruptures occurred in the fault hangingwall as discrete fracture systems with
219 lengths ranging from 0.5 m up to 530 m, and width from a few meters to more than 50 m. At the
220 outcrop-scale, the fault slip is accommodated by a variety of geomorphic features denoting the
221 high degree of complexity of the deformation zone [details in *Cucci et al.*, 2019]. Briefly, dip-slip
222 components are marked by smoothed scarplets especially in the hidden section of the FF (Figure
223 4a), while strike-slip components are revealed by *en-échelon* left-stepping ruptures or clearly
224 expressed by purely right-lateral displacements (Figure 4b,c). Extensional and compressional
225 components of displacement appear in the form of grabens, open fractures or pressure-ridges,
226 respectively (Figure 4d-f). Locally, a kinematic partition of the slip components is present, with

tensional open fractures or normal faulting and strike-slip ruptures set at the top and base of the fault escarpment, respectively (Figure 4c).

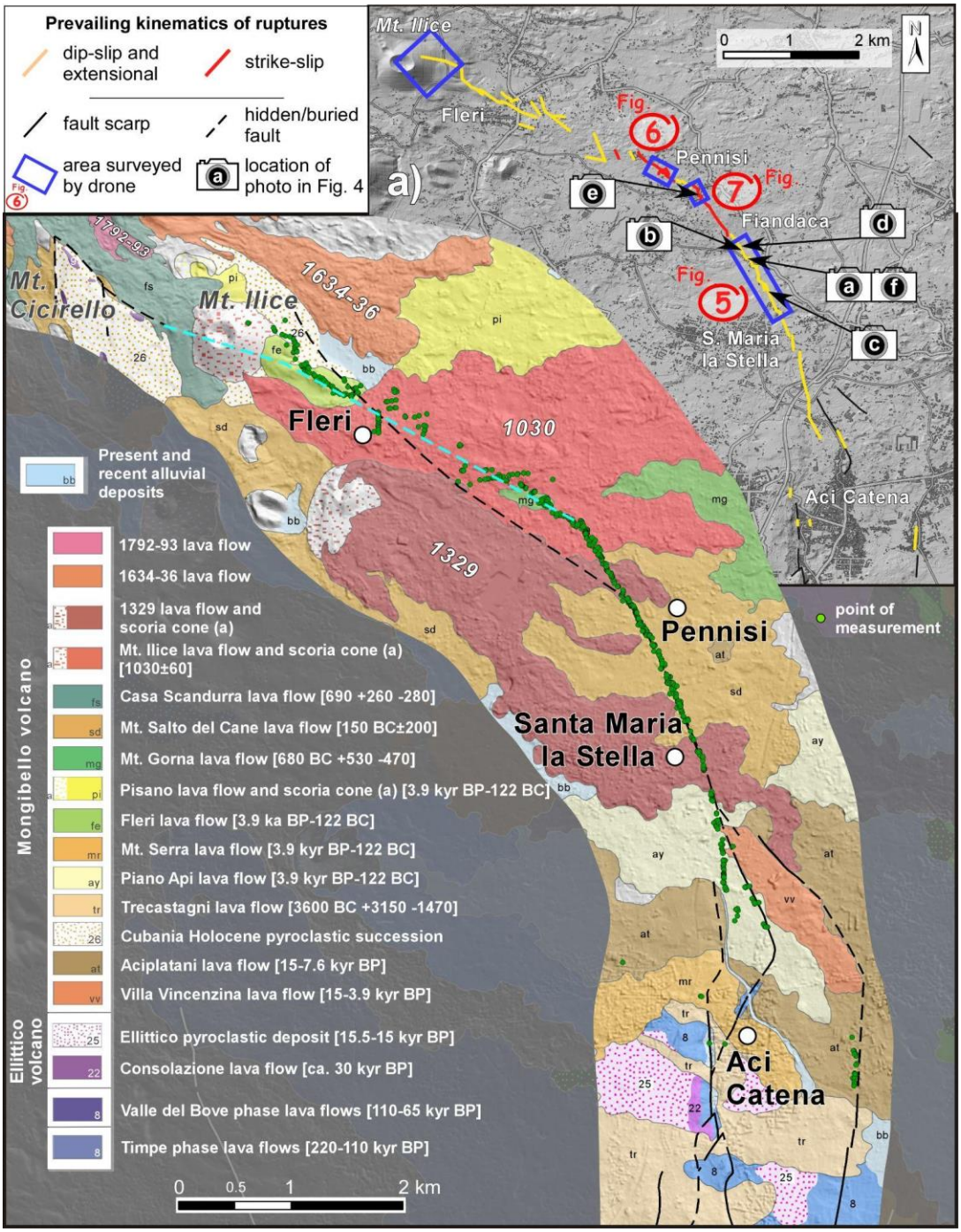

Figure 3. Geological map of the zone crossed by the 26 December 2018 surface ruptures [dark green dots, from *Villani et al.*, 2020] along the two sections of the Fiandaca fault [modified after *Branca et al.*, 2011a]; the new trace of the hidden section is marked by the hatched light green line. The inset (a) shows the location of photos and figures of this work along the coseismic ruptures [simplified from *Civico et al., 2019*].

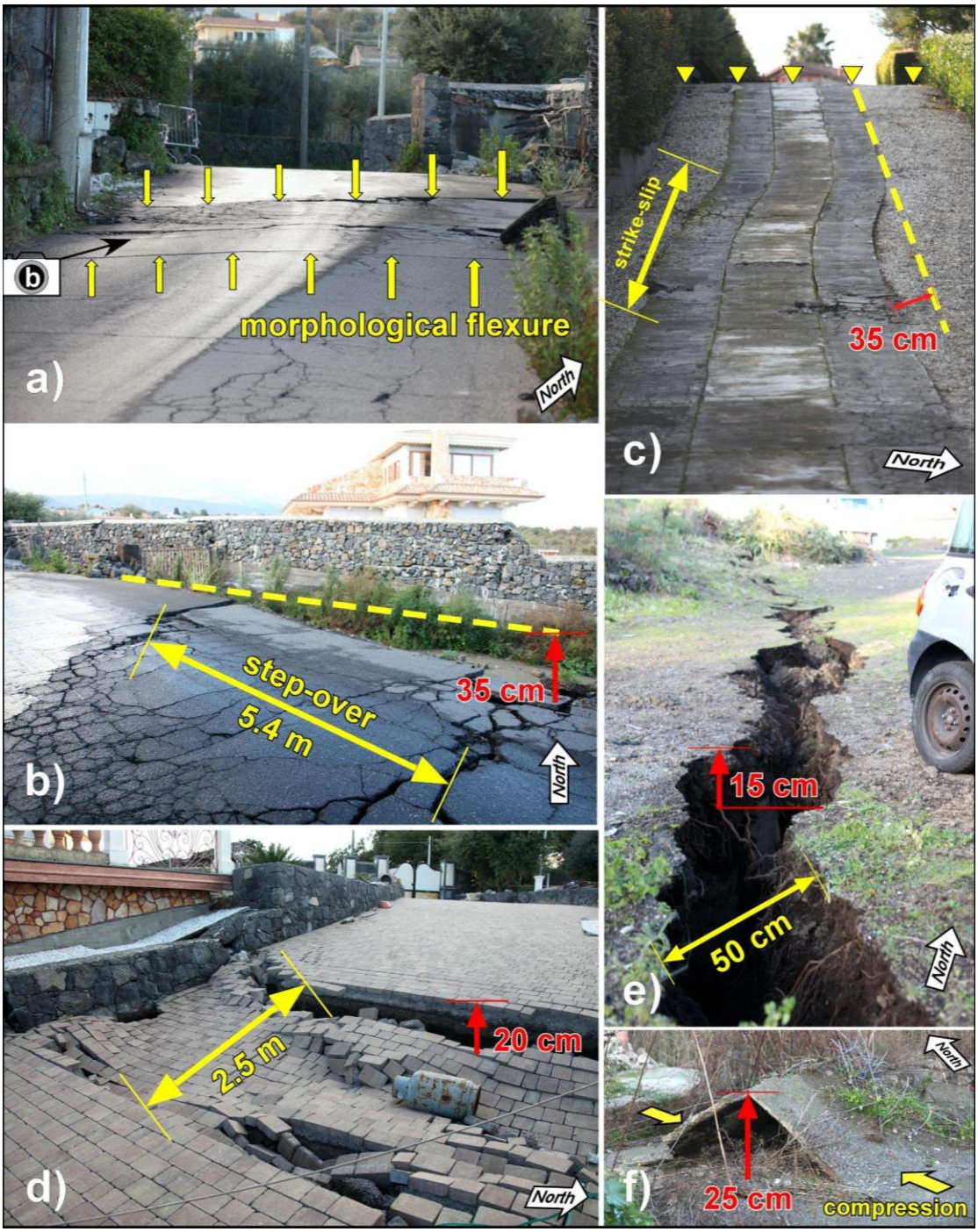

Figure 4. Examples of geomorphic features produced by the coseismic deformation (primary faulting). (a) Field evidence of the earthquake fault along the hidden section of FF: note that the smoothed scarplet (morphological flexure) accommodates the vertical component of slip in a 6 m-wide strip; letter (b) in the black circle indicates photo location within Figure 3. (b) Detail, *en-échelon* left-stepping ruptures. (c) Right-lateral displacement; yellow triangles point to the tensional open fractures at the top of the fault escarpment. (d) Graben. (e) Open fracture. (f) Angular-ridge type mole-track on concrete pavement.

3.2 Surface rupture pattern

The expression of the coseismic rupture is analyzed here by exploiting the high-resolution SfM photogrammetry obtained by the drone surveys [details in *Civico et al.*, 2019]. The integration of the geo-referred aerial mapping with the closely spaced dataset of field measurements allowed us to unscramble the kinematic features of faulting at different observational scales.

At the outcrop scale (centimeters to tens-of-meters scale), the coseismic faulting tends to mimic a mole-track expression [*sensu Jackson*, 1997] formed by the humping up and cracking of the ground. Specifically, we recognised two different geomorphic features: (i) angular-ridge type mole-track developed on rigid ground surfaces, typically man-made structures (Figure 4f); (ii) bulge-type mole-track, developed within unconsolidated to weakly consolidated coarse-grained deposits (i.e. volcaniclastic soil or weathered and colluviated volcanic tuff deposits) that overlay a rigid bedrock (i.e. lava flow bedrock), as observed in analogical deformation experiments [e.g. *Tchalenko*, 1970; *Wilcox et al.*, 1973; *Naylor et al.*, 1986; *Withjack and Jamison*, 1986].

In general, the surface faulting appears composed of several elements, 1 to 15 m wide and 10 to 50 m long, characterised by centimetric to metric structural features with variable orientation and kinematics. Figure 5a shows an illustrative expression of a single displacement zones (hereinafter SDZ), where the dominant structural features are: (i) overstepping, *en-échelon* array of left-stepping tensional open fissures (orthogonal opening ≥1 cm, throw <1 cm, strike-slip <1 cm or not identifiable); (ii) hybrid (opening ≥1 cm, throw ≥1 cm, strike-slip not identifiable or <1 cm); (iii) transtensional right-lateral fractures (opening ≥1 cm, throw ≥1 cm, strike-slip ≥1 cm). At places these structures, accommodating most of the deformation, interconnect to form a sawtooth trajectory. Secondary structures are the right-stepping arrays of transpressive (opening <1 cm, throw >1 cm, strike-slip >1 cm) and reverse fractures (opening <1 cm, throw >1 cm, strike-slip <1 cm or not identifiable), rarely accompanied by compressional fold axes and left-stepping arrays of right-lateral strike-slip fractures (opening <1 cm, throw <1 cm, strike-slip >1 cm). Scarcely represented are the strike-slip, transtensional and reverse fractures with left-lateral kinematics. As a whole, the SDZs appear to have transtensional kinematics, where the prevailing tensional component is often expressed by gravity grabens that emphasize the fracture opening values (see profile A-A' in Figure 5b).

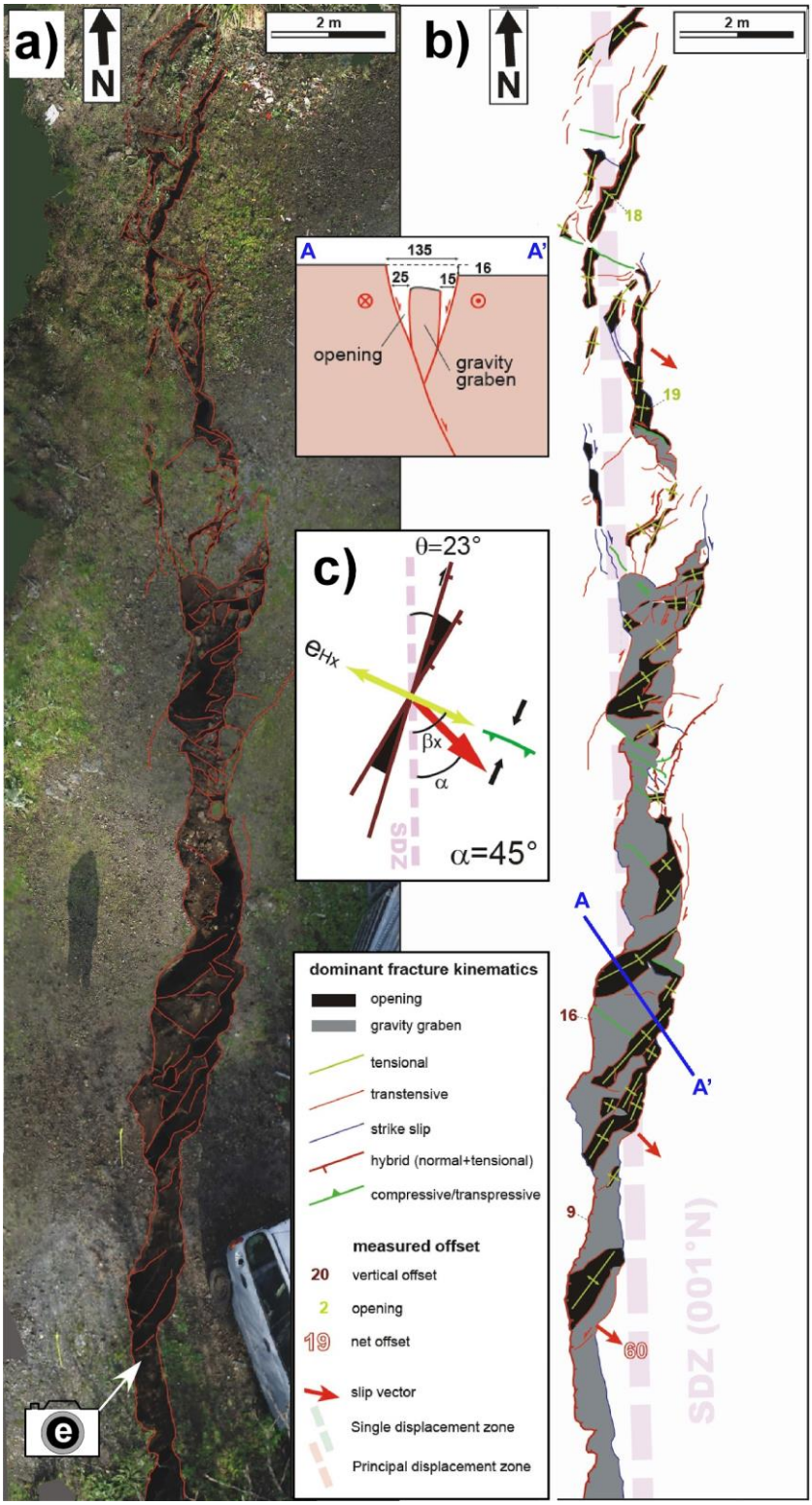

Figure 5. Example of outcrop-scale rupture pattern interpretation of a transtensional SDZ with evident tensional component (see Figure 3a for location). (a) Zenithal view of the area by means of orthophoto derived from drone photogrammetry. The trace of the main ground failures is reported in red; letters indicate the location of photos shown

in Figure 4. (b) Scheme of the rupture elements with their kinematic interpretation. The values of the measured offsets (net slip and its components) and slip vector trends are reported. Thick dashed lines represent the local average strike of SDZ. (c) Theoretical fault trends and kinematics expected in a transtensional infinitesimal strain [from *Withjack and Jamison*, 1986] consistent with the observed structures. The cross-profile A-A' sketches out the geometrical relationship among throw, heave and tensional opening of the gravity graben.

At the intermediate scale, corresponding to tens to hundreds-of-meters scale, the *en-échelon* left-stepping SDZs in general dominate the surface faulting pattern (Figure 6). The surface faulting pattern shows infrequent right-stepping compressional features (e.g. thrusts, transpressional structures, push-ups and hingeline-flexure tensional cracks) that concentrate in the SDZs stepover transfer zones, where the compressional components of the simple shear converge.

Notably, only sparse clear P-shears or Y-shears (parallel to the SDZ) can be observed, whereas several incoherent or complex anastomosing patterns can be attributed to the interference of the surface faulting with man-made structures (tarmac roads, buildings, pavements, etc.). Occasionally, the surface faulting pattern is also impaired by the presence of pseudo-lateral spreadings following the collapse of retaining walls. Locally, the SDZs appear organized in variably overlapping, *en-échelon* left-stepping arrays of structures.

Figure 7a shows an exemplary situation where these features are spaced 5 to 30 m apart and, due to the presence of important vertical components of slip, they separate stripes of relative coseismic subsidence and uplift with a horst-and-graben structure. At places, the deformation zone exceeds 100 m in width. In other sites where the long-term fault scarp (i.e. scarp built by the repetition of multiple coseismic slip in past surface-rupturing earthquakes) is preserved, we observed a kinematic partition of the coseismic offset, with the SDZs accommodating most of the right-lateral component at the base of the scarp and the tensional component in the footwall (Figure 4c).The envelope of the SDZs *en-échelon* arrays defines a principal displacement zone (hereinafter PDZ) at a kilometer scale, which strikes with a divergent orientation (Figure 6b and 7b) and represents the surface expression of the seismogenic slip plane.

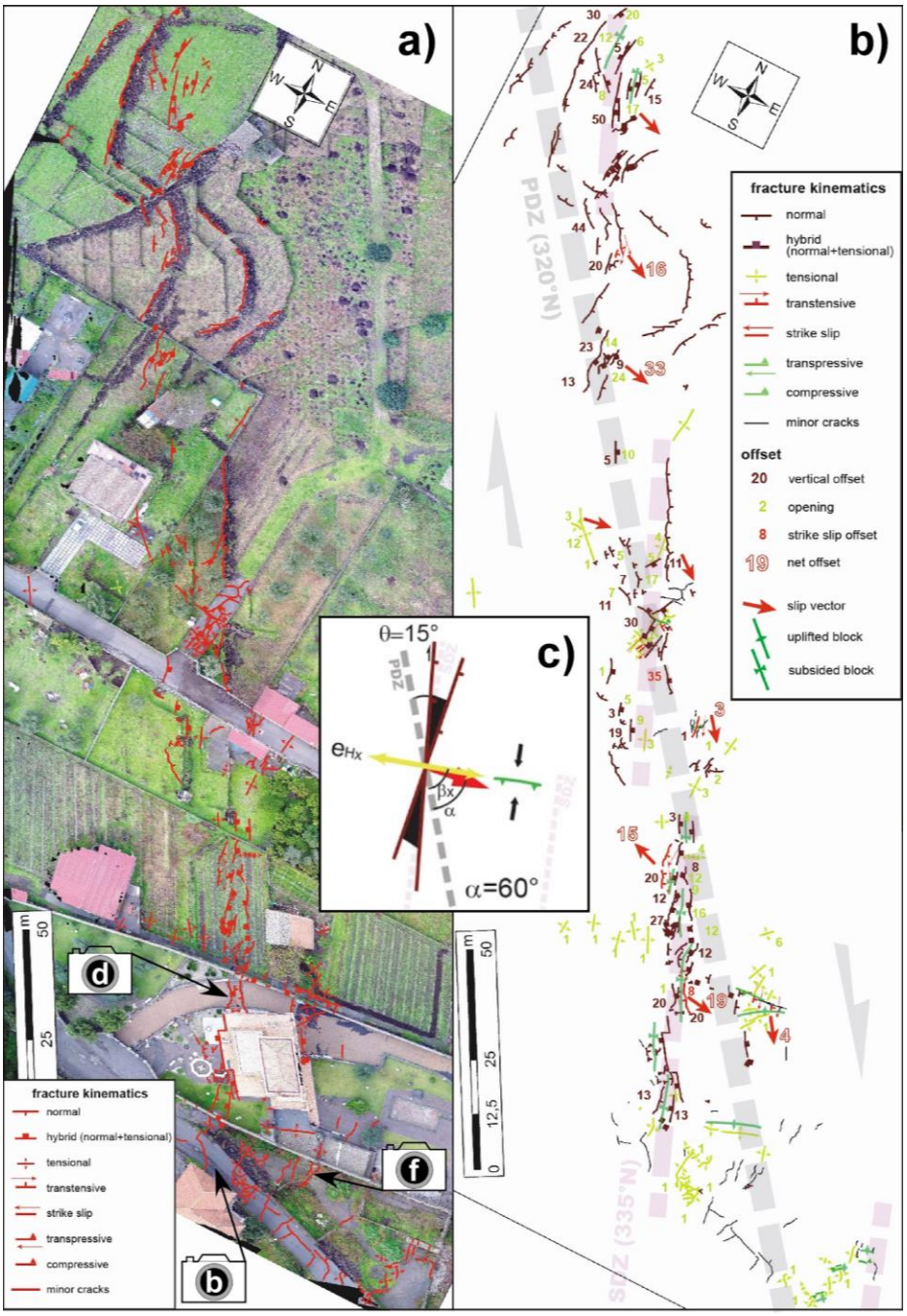

Figure 6. Example of the hundreds-of-meters scale faulting pattern and SDZs geometrical organization (see Figure 3 for location). (a) Zenithal view of the area by means of orthophotos derived from drone photogrammetry. The trace of the main ground failures is shown in red; letters indicate the location of photos shown in Figure 4. (b) Scheme of the rupture elements with their kinematic interpretation. The values of the measured offsets (net slip and its components) and slip vector trends are reported. Thick dashed lines represent the local average strike of PDZ and SDZ; green lines symbolize the axes of relative subsidence or uplift among SDZs (see text for explanation). (c) Theoretical fault trends and kinematics expected in a transtensional infinitesimal strain [from *Withjack and Jamison*, 1986] consistent with the observed structures.

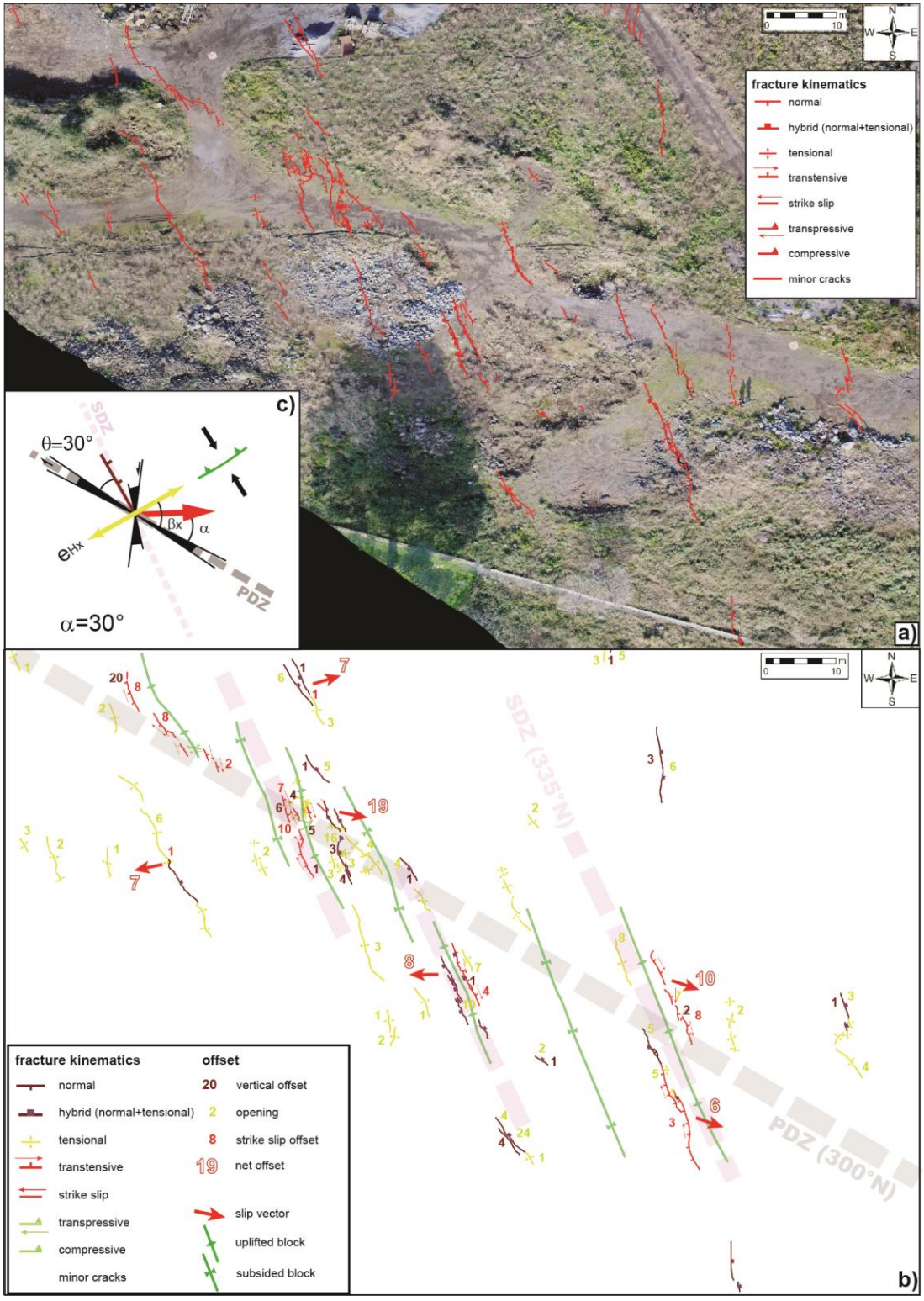

311

312 **Figure 7.** Example of the hundreds-of-meters scale faulting pattern and SDZs geometrical organization (see Figure 3
313 for location). Explanation as in Figure 6.

314

315 The recognition of piercing points (i.e. formerly adjacent points on the opposite sides of a
316 fault) allowed us to measure the net displacement of the fractures, as well as to determine the
317 orientation of the slip vectors of the coseismic movement. Most of the collected slip vectors are
318 almost orthogonal to the observed tensional fractures and parallel to the major axis of the
319 theoretical infinitesimal strain ellipse responding to the local transtensional SDZ strain
320 arrangement (e_{HX} in Figure 5c). The structural elements, with a few exceptions, represent a right-
321 lateral simple shear fairly well, suggesting the presence of a strike-slip component even along
322 failures for which it was not identifiable in the field, coupled with a significant pure shear
323 component (Figure 5b). At the kilometer scale, the SDZs appear to constitute a synthetic Riedel
324 system of the theoretical infinitesimal strain ellipse responding to a complex dextral fault zone.
325 Notably, the SDZs show angles with the PDZ, along with those of slip vectors, varying with respect
326 to the theoretical infinitesimal strain ellipse of simple shear (Figure 6c and 7c).

327 ***3.3 Along-strike distribution of the surface rupture features***

328 The geometric, kinematic and displacement characteristics of the surface rupture are
329 described here, considering separately the northern and southern sections of the FF as indicated in
330 Figure 3. The original structural data from *Villani et al.* [2020] have been elaborated (e.g.
331 aggregating the slip components to obtain a spatially denser net slip dataset) and we expanded
332 their previous analysis, focusing on the spatial changes of the geometric and kinematic features
333 along the strike. In Figure 8a, the rose diagrams represent the trends of: fractures measured in the
334 field (red petals), slip vectors obtained from the piercing points (pale green petals), SDZs inferred
335 from the analysis of the drone photogrammetry (pale violet petals), PDZ as a whole (grey bars).

336 In detail, a different arrangement of the ruptures is evident in the two sections of the FF
337 fault. The northern section, characterised by a N310°-striking PDZ, displays a modal peak of SDZs
338 trending N315° and coseismic fractures broadly trending N335°, with a secondary peak of N320°.
339 The coseismic slip vectors consistently trend N115°, but a secondary peak at N060° is also evident.
340 These data indicate a prevailing right-lateral kinematics with minor dip-slip components
341 downthrowing to the northeast. The southern section is characterised by a general clockwise
342 rotation of the overall fracture pattern: the PDZ is aligned along a bearing of N335°, while the
343 SDZs broadly trend N335°-355°; the measured fractures concentrate around the northern quadrant
344 with two directional peaks at N345° and N355°. Finally, the slip vector trends are not uni-modal,

rather they range from N100° to N145°. This arrangement indicates a higher degree of complexity of deformation along the southern section of the FF compared to the northern one.

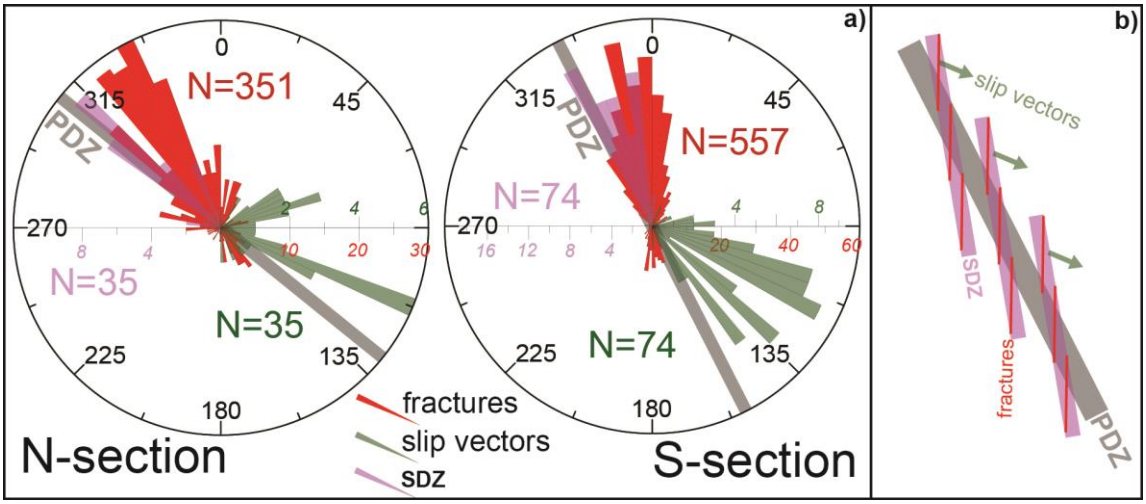

Figure 8. (a) Rose diagrams showing the orientation of coseismic surface rupture strands, slip vectors, SDZs and PDZ for the two sections of FF. (b) Schematic diagram showing the geometrical relationships among the different ranks of structural elements forming the PDZ shear zone.

The mutual geometric relationships among PDZ, SDZs, individual fractures and slip vectors are sketched in Figure 8b. A general scale-dependent rotation of each set of fractures is evident, showing clockwise changes in the strike from the first order rupture zone to the individual features of a lower rank. Looking at the spatial distribution of these data, in the following we analyse how kinematics and coseismic displacement vary along the strike, and relate them with the field evidence of deformation documenting the complexity of the rupture.

In Figure 9a, we project the collected offset data onto a baseline that represents the simplified trace of the coseismic rupture, i.e. the PDZ, obtained by interpolating the pattern of the main SDZs (cfr. Figure 3). The slip vectors are indicated by black arrows pointing to the direction of movement of the eastern fault block; the location of the mainshock epicenter is also reported. Clearly, the fracture trends concentrate in two narrow directional domains (N300°-360° and N000°-020°) along the entire rupture (Figure 9b). A subordinate trend (N150°-180°) is represented by a diffuse set of oblique fractures that develops at the tips of major strands or in overstepping sectors between sub-parallel and nearly N-trending ruptures. Both directional domains of fracture trends appear to slightly rotate clockwise to the south. Although less abundant than offset data, the slip vectors (Figure 9c) also show a perceivable change in direction along the strike, namely

N080°-120° in the northern sector and N100°-140° in the southern one. We also calculated the divergence angle between the direction of the slip vectors with respect to the local SDZs (Figure 9d). Null deviation (0°) would indicate a perfectly strike-slip kinematics, while we notice that the angular difference α is positive almost everywhere with few exceptions.

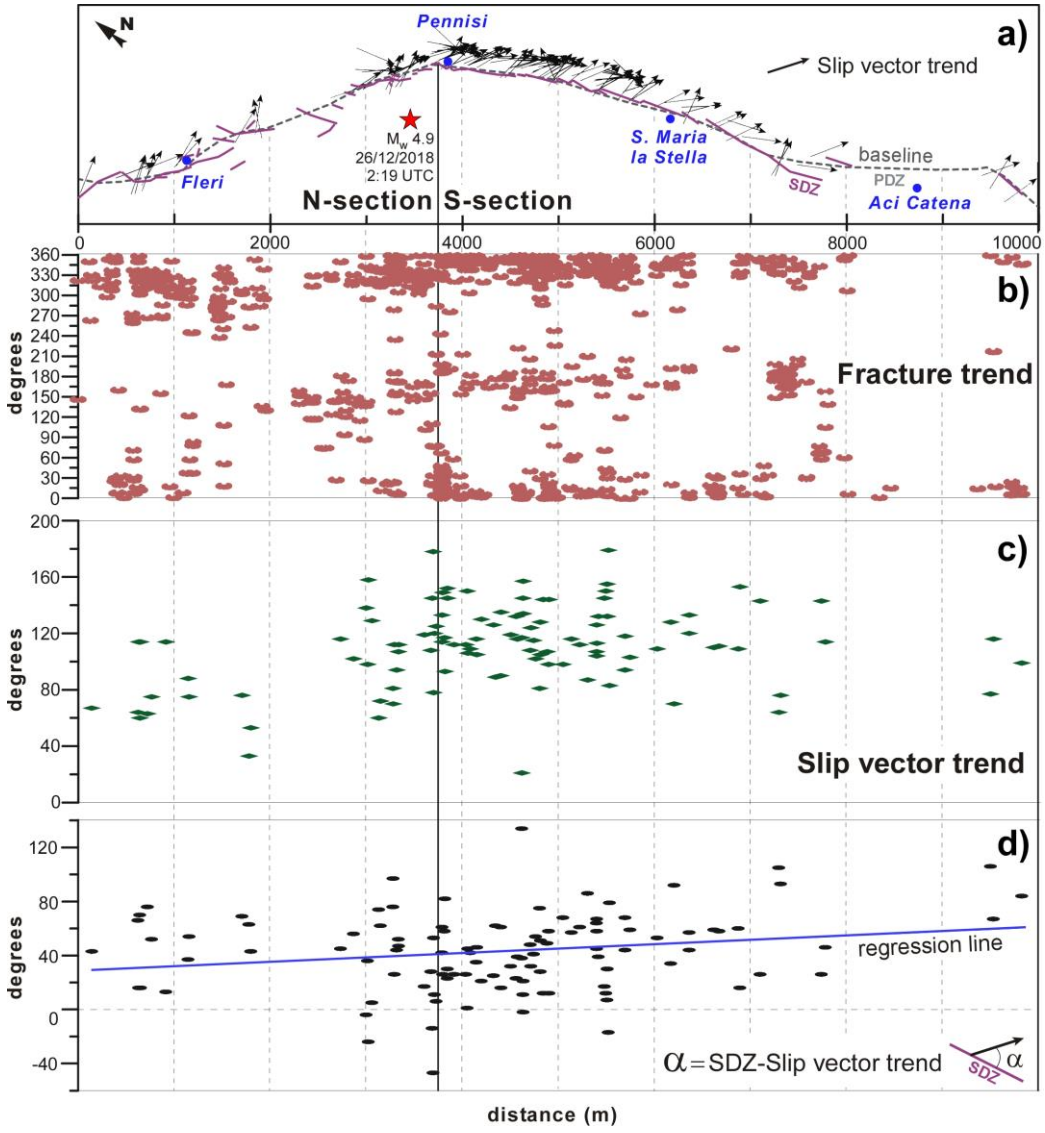

Figure 9. Diagrams showing the variations (degrees) of the kinematic features projected along the two sections of FF (marked by the vertical black line). (a) The grey baseline represents the simplified trace of the coseismic rupture trace (PDZ), obtained by interpolating the pattern of the main SDZs (cfr. Figure 3); the red star indicates the epicenter of the 2018 earthquake. Spatial distribution of (b) trend of the fractures, (c) strike of the slip vectors, (d) divergence angle (α) between local SDZs and slip vectors.

In particular, most data show deviations larger than 10° and up to 80°-100°, indicating that the sense of movement of the downthrown block is consistently towards the eastern sector, and the dip-slip component increases towards the south. Regarding the slip distribution, in Figure 10a we projected the offset data along the baseline together with the main volcanic formations (lava flows and pyroclastics, coloured bars sketched from Figure 3b) outcropping along the rupture trace in order to consider the possible effects of lithology. We note that the net offset (Figure 10b) shows an isolated peak of 30 cm at the northern tip of the FF and a broad region of high values, with a maximum of 33 cm between Pennisi and S. Maria la Stella, where the background value is typically about 15 cm.

In the case of the strike-slip component (Figure 10c), we indicated the contribution of each single splay rupture and the sum of the overstepping splays. We additionally showed the envelope of local maxima, and the distribution curve resulting from a running average smoothing of the cumulative offset in overstepping zones (window size of 100 m). Overall, also the lateral component of displacement shows a pattern similar to the net offset data (Figure 10b). We believe that the gravitational effects would not have significantly affected the horizontal component of movement during (or soon after) the earthquake, therefore the maxima envelope curve provides a reliable picture of the strike-slip distribution along the strike. Notably, the main patch, with a peak of 35 cm, is about 1.5 km long and located very close to the projected epicenter location. The vertical component of slip is a little more scattered (Figure 10d), however the broad area of maximum overlaps the zones of maximum net slip and strike-slip offsets. As noted by *Villani et al.* [2020], this may indicate that the rupture process was characterized by a directivity to the south and that the hypocentre is located at the borders of a large asperity that was subsequently broken during the mainshock. Unfortunately, to date there are no seismological studies investigating these particular aspects of the seismic source.

Finally the opening component (Figure 10e) requires a careful analysis of the local complexities due to shallow gravitational effects induced by the shaking. Although characterised by the same general pattern, local peaks exceeding 60 cm are located considerably to the north of the area affected by the maximum displacement (for both net slip and strike-slip components).

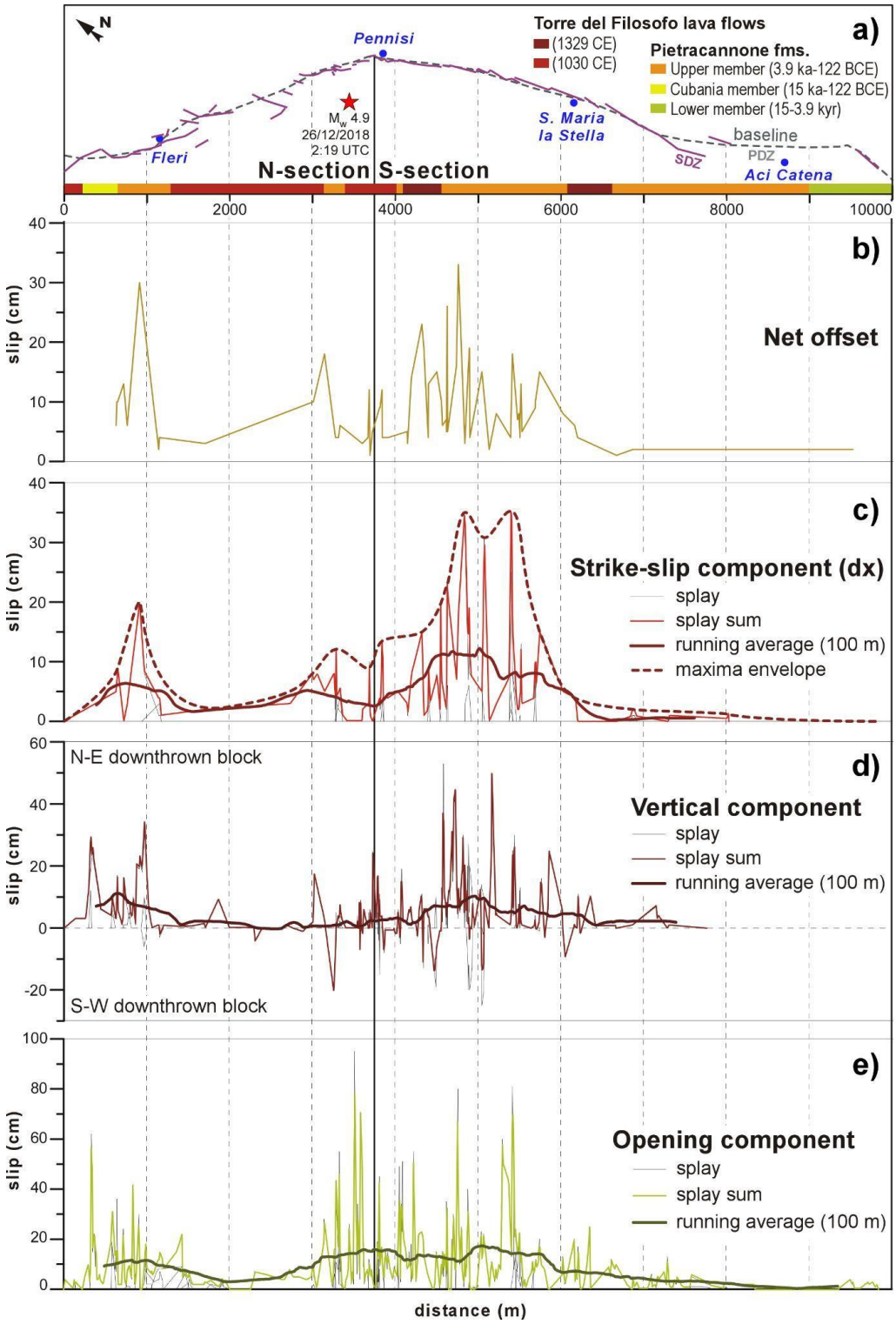

Figure 10. Line-scatter plots [data from *Villani et al.*, 2020] showing the variations of the components of coseismic slip projected along the two sections of FF (marked by the vertical black line). (a) The baseline is here represented with the volcanic formations displaced by the coseismic rupture. Spatial distribution of (b) net offset, (c) strike-slip, (d) vertical and (e) opening components. Note that the vertical axes are not in scale.

The gravity-graben features already described for the site of Pennisi (Figures 4e and 7), are interpreted as offset-landforms morphologies overlying a strike-slip structure in a transtensional strain configuration, where the resulting opening component orthogonal to the fracture walls, accommodates the collapse of the shallow soil layers.

4 Discussion

In the following, we analyse the field measurements and correlate them with other findings obtained from different methodological approaches. Our goals are: 1) to describe the faulting characteristics by zooming out from the scale of the individual rupture episode; 2) to discuss the long-term expression of the fault; 3) to provide clues on its growth and segmentation and 4) to propose a conceptual model of fault behaviour with implications on local, fault-based seismic hazard.

4.1 Kinematics of the 2018 earthquake rupture

The kinematic interpretation of the 2018 earthquake from the geological point of view is constrained, in great detail, by the numerous measurements acquired in the field that ensure a high spatial completeness of the survey. However, the complexity of the rupture requires a critical evaluation of the data to infer a reliable coseismic faulting mechanism. While the overall pattern of the SDZs outlines the fault location, at the outcrop scale the SDZs are not indicative of the trend and kinematics of the fault plane at a seismogenic depth, possibly due to mechanical discontinuities, as hypothesized also by *Tortorici et al.* [2021]. In general, the prevalence of tensional or compressional structures in the mole-track points to transtension or transpression, respectively, but locally they can respond to a local strain reorganization as well. Similarly, the field-collected slip vectors refer to the kinematics of the structures inside the SDZs, and are not fully representative of the first-order fault block motions.

Most of the SDZs have transtensional kinematics. Taken together as synthetic Riedel systems, they indicate important opening and dip-slip components of movement, and several fractures diverging from the ones predicted by the Andersonian model of faulting indicate a deviation from theoretical simple shear. The overall surface rupture pattern appears to describe an infinitesimal 3D strain derived from the combination of a pure shear coaxial extension and a non-coaxial wrench simple shear, generated by an oblique displacement with angle α to the FF deformation zone boundary fault (red arrow in Figure 11a, right panel) [e.g. *De Paola et al.*, 2005].

In detail, the individual surface rupture patterns are typically characterized by quadrimodal sets of normal-oblique faults trending at low angles to the deformation zone boundaries; in particular for $\alpha > 30°$ the increasing pure shear component causes a progressive reduction of the angle θ between the boundary fault and the principal synthetic fracture planes (Figure 11b) [e.g. *Withjack and Jamison*, 1986].

From the 2018 earthquake rupture pattern, we reconstructed the angle θ between fractures and SDZ in the key area of Figure 5, and between SDZs and PDZ in the key areas of Figures 6 and 7, as representative of the two differently oriented FF sections (see inset of Figure 3 for location). In all these cases, the values enable obtaining oblique angles of displacement α of 30°, 45° and 60°, increasing from north to south (see Figures 7c, 5c and 6c, respectively). In compliance with the Poisson's ratio of basalts (Figure 11c) calculated for the study area [*Aloisi et al.*, 2011], these divergence vectors mostly produce an extension-dominated transtension (Figure 11d), where the minimum principal extension axis switches from the horizontal orientation to the vertical one. This rotation produces an increase of the normal faulting component southward along strike, as observed also by *Romagnoli et al.* [2021].

As observed for many large earthquakes, at the fault scale the PDZ represents the surface expression of the fault plane localized at a seismogenic depth (e.g. Dast-e Bayaz 1968 [*Tchalenko and Ambraseys*, 1970; *Tchalenko and Barberian*, 1975]; Landers 1992 [*Sieh et al.*, 1993; *Johnson et al.*, 1994; *Lazarte et al.*, 1994]; Duzce 1999 [*Pucci et al.*, 2006]). In Figure 12, we plotted the oblique displacements reconstructed for the key areas of Figures 5 and 6, on the same baseline representing the PDZ. Although the relevant angles α of displacement are significantly different from each other – 30° in the northern section vs. 60° in the southern one – the vectors appear almost parallel in the map (red arrows). A quasi-rigid behaviour of the crustal fault blocks is suggested by the near-parallel vectors, although the FF shows a prominent releasing bend near Pennisi (25° clockwise strike change).

Notably, the far-field displacement maps of the 2018 seismic event from DinSAR data [*De Novellis et al.*, 2019] show the strike slip component of the two fault blocks (observed in the E-W direction) reaching a relative displacement of 35 cm, very similar to the near-fault measurements (Figure 10c) but with higher values being centered near the Pennisi village, and a distribution of the displacement elongated in agreement with the divergence direction (arrows) of the two fault blocks (Figure 12b).

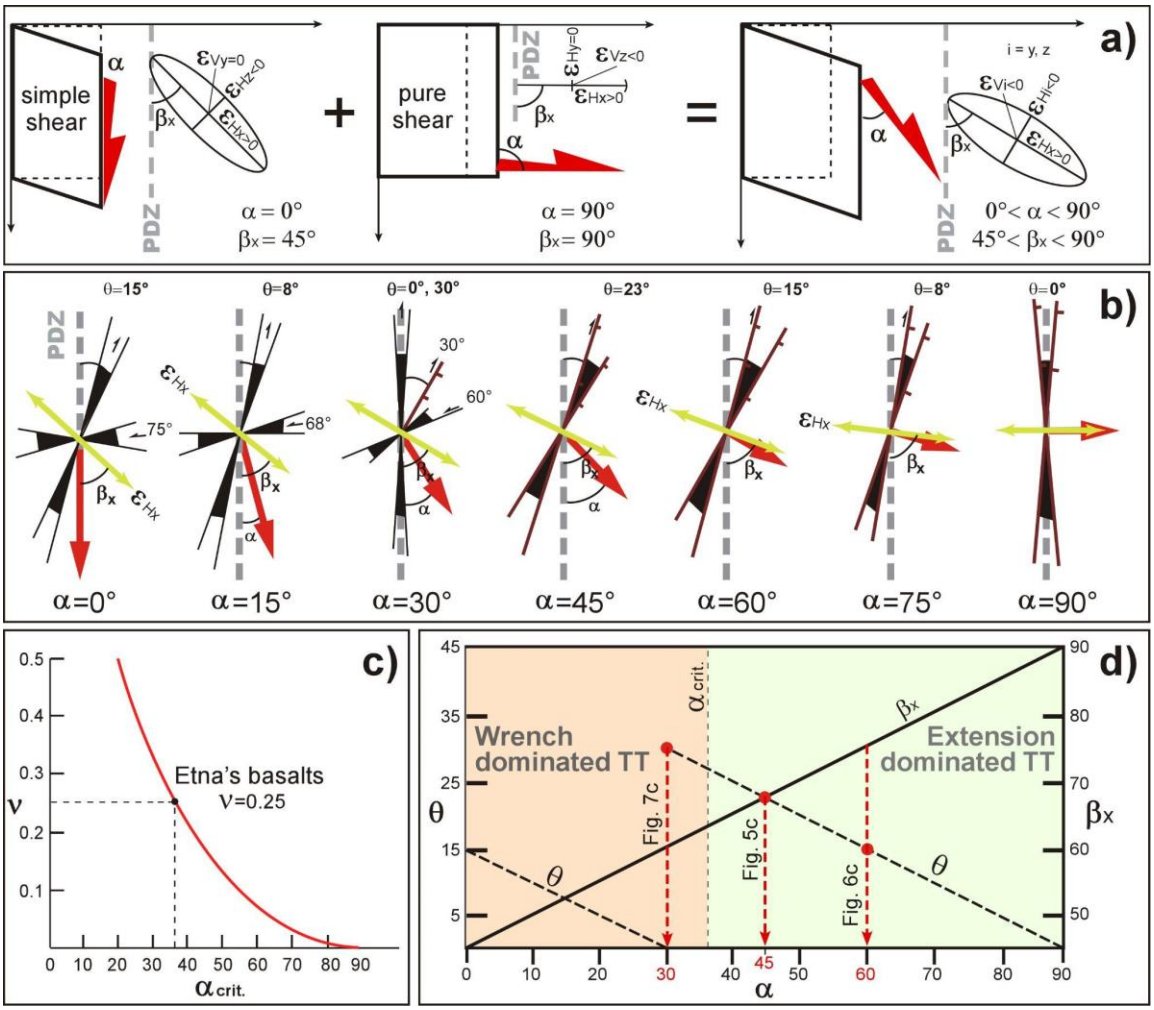

Figure 11. (a) Sketch of the infinitesimal 3D, non-coaxial transtensional strain derived from the combination of plane strain simple shear wrench deformation and plane strain pure shear coaxial extension. The theoretical strain ellipses are reported: $\varepsilon_{Hi} = \varepsilon_{Hz}$ and ε_{Hy} for wrench- and extension-dominated transtension, respectively; β is the angle between the maximum horizontal extension axis and the boundary fault; α is the divergence angle between the displacement and the boundary fault; x, y and z are the maximum, intermediate and minimum infinitesimal extension axes [from *De Paola et al., 2005*]. (b) Rose diagrams of model-predicted fault trends produced by combining extension and right-lateral shear with respect to the PDZ trend. The red arrow indicates the relative displacement direction between opposite sides of the PDZ and the green arrow is the direction of the largest extensional strain axes (ε_{Hx}). Prevalent strike-slip conjugate and normal faults (hachured) trends are reported along with main angles to the PDZ (θ is the angle between the boundary fault and the principal synthetic fracture planes) [from *Withjack and Jamison, 1986*]. (c) Graph of Poisson's ratio □ versus α_{crit} (the threshold angle between wrench- and extension-dominated transtension); the mean value □ for the Etna's basalts [from *Aloisi et al., 2011*] is also indicated. (d) Diagram of the predictable relationship existing between the angle α and the angles β and θ. α angles of key areas of the 2018 earthquake surface faulting (Figs. 5c, 6c and 7c) are reconstructed from θ's measured on the rupture patterns (red dots).

The far-field vertical component shows maxima of the relative displacement between the two fault blocks reaching 15 cm, in accordance with the near-fault averaged value (Figure 10d), along the unclamping southern section of the FF (Figure 12c).

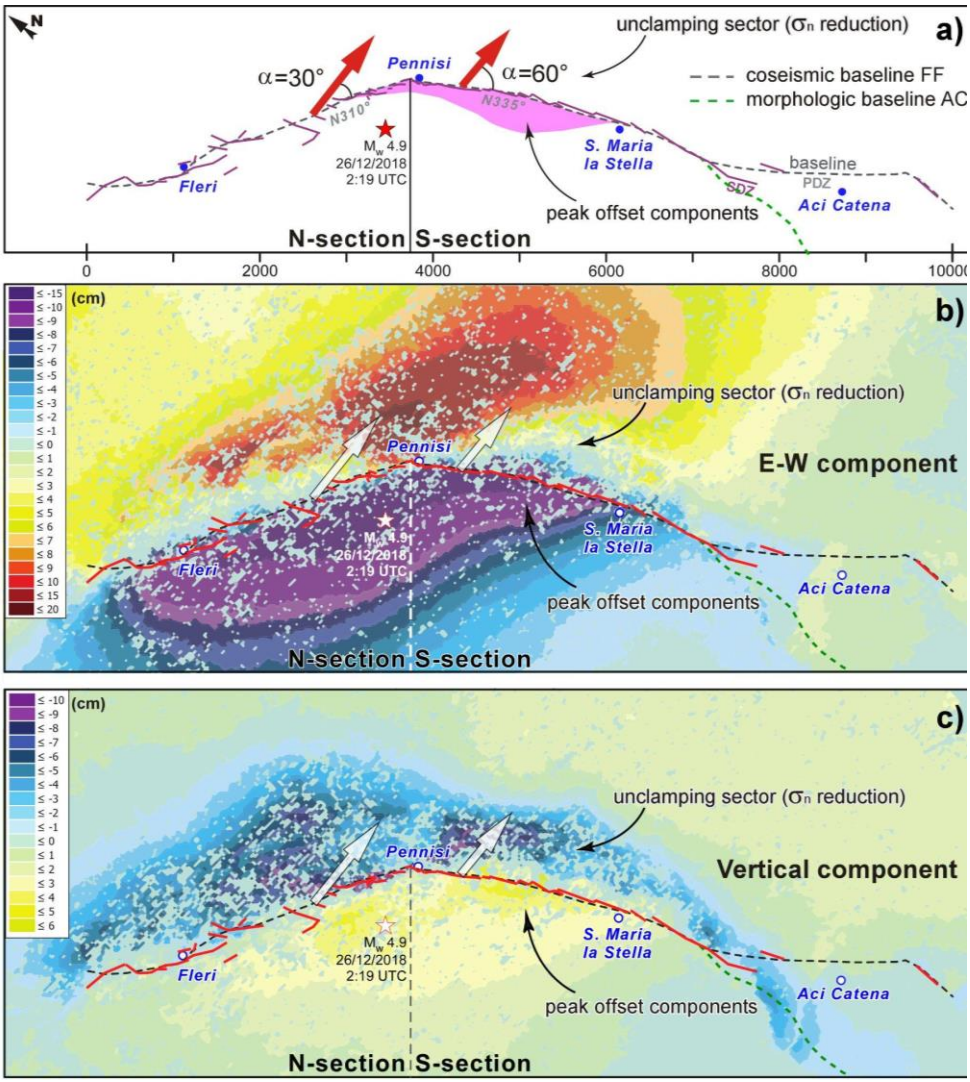

Figure 12. a) Conceptual relationship between the boundary fault trend change (PDZ) and the divergence angles α derived from the surface faulting pattern analysis. The along-strike distribution of the slip (both vertical and strike-slip components) is indicated in purple (area approximately proportional to the offsets). Comparison among the FF surface fault trace and (b) the E-W and (c) vertical far field displacement maps, computed by exploiting the ascending and descending Sentinel-1 measurements from DInSAR analysis [modified from *De Novellis et al.*, 2019].

A particular feature of the DInSAR displacement maps is the coseismic dislocation (a few centimeters of vertical motion) extending south of the FF tip, along the northernmost part of the ACF escarpment. Here, because of low and diffused deformation, no coseismic ruptures were

observed in the field apart from a few rare, minor off-fault fractures mapped in the village of Aci Catena (cfr. Figure 3).

4.2 Long-term morphologic expression

In the following, we analyse the 2018 rupture event from the standpoint of the geological process producing the long-term morphological expression of FF. To this end, we traced a series of topographic profiles astride the PDZ to capture any morphological feature related with the long-term activity of the fault. For this analysis we used the topographic dataset by *Gwinner et al.* [2006] that consists of a high-resolution 1-m grid DEM, providing excellent detail, among which many micro-topographic features due to manmade buildings and modifications to the land. To overcome this drawback, we applied a low-pass filter and then resampled the DEM to a coarser pixel size (2 m) in order to obtain a smoother surface. The location of the topographic profiles (Figure 13a) was then carefully selected in order to avoid the areas subject to extreme morphological alteration, therefore their spacing along the fault strike is uneven, and some zones of the northern sector of the FF were excluded (e.g. the first 800 m and the fault section at x=1800-3000 m). In this way, we obtained 51 profiles allowing a reliable reconstruction of the fault scarp height, which can be considered as a good proxy to reconstruct the vertical component of the long-term fault displacement. The variable length of the topographic profiles (200 to 600 m) was tuned in order to contain sufficiently large and representative portions of morphologic surfaces preserved in the footwall and hangingwall blocks, assumed as being originally continuous. Uncertainty in the fault scarp estimate was evaluated taking into account and summing the standard deviation of the footwall and hangingwall morphological surfaces with respect to their best-fit linear regression curves.

The shape of the FF scarp height curve (Figure 13b) tapers gently towards the north and the south, whereas in the central and southern sectors (x = 3500-7000 m) it displays a broad peak with a maximum height of 19.9 ± 0.8 m. In general, apart from the exhumation processes due to erosion as highlighted by *Catalano et al.* [2013], the original (i.e. undisturbed) morphological throw is modified by a number of lava flows crossing the fault (Figure 3), which smooth or even hide the scarp (see the buried and hidden morphotectonic features discussed in *Azzaro et al.*, [2012]. This situation has significantly contributed to reducing the morphological throw in the southern section of the fault (x = 5000-7000 m), and to conceal any morphological evidence of the

escarpment in the northern section (x = 0-3000 m). This also explains why the 2018 PDZ does not correspond to the hidden trace of the FF that was mapped before this event only through the historical accounts of past earthquakes [*Azzaro, 1999*; Figure 3].

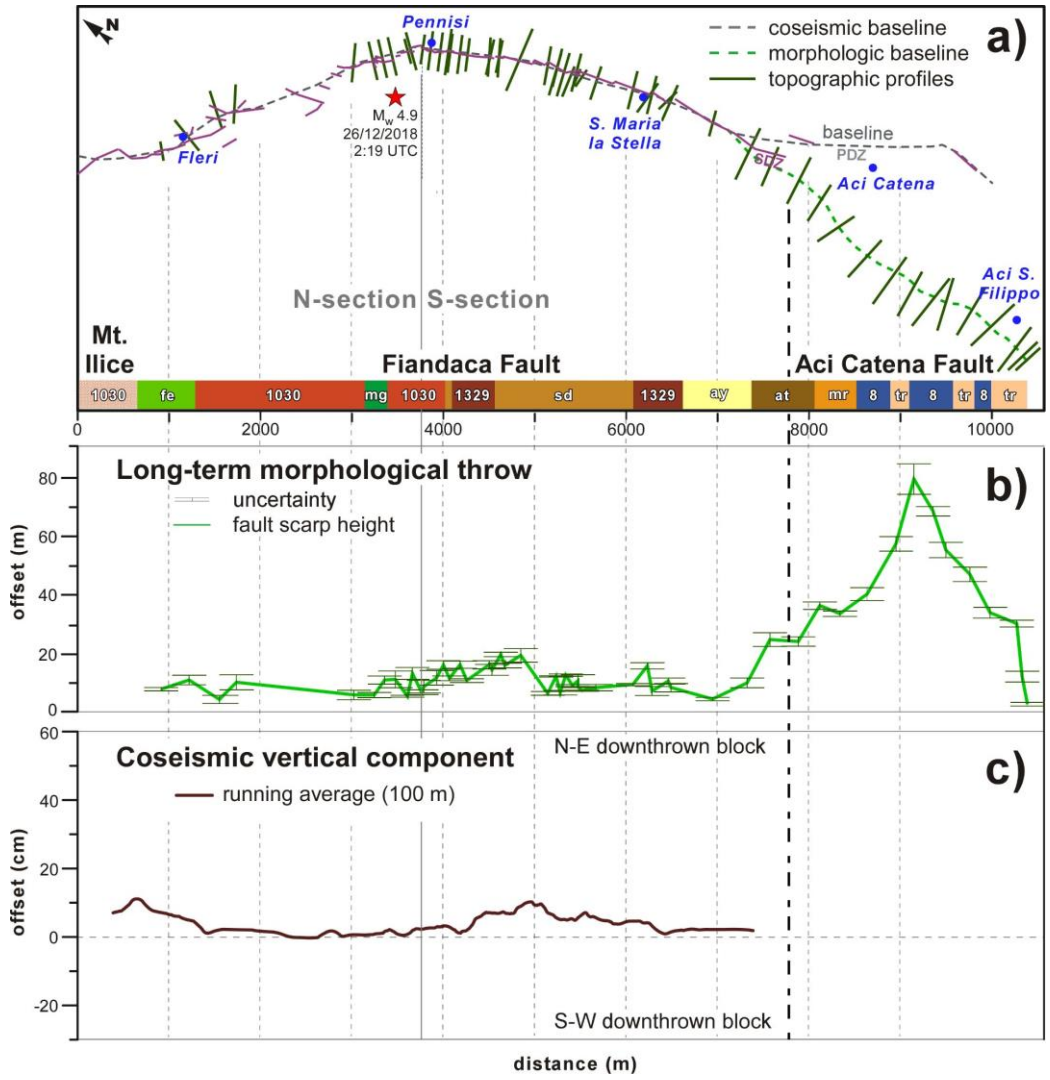

Figure 13. Line-scatter plots showing the distribution of the cumulative fault scarp height (i.e. morphological throw) compared to the vertical components of coseismic slip projected along the FF (marked by the vertical black line). (a) The FF baseline is extended southward, along the prominent fault escarpment of the ACF. The volcanic formations displaced along the baseline are also indicated (cfr. Figure 3 for details) together with the location of the topographic profiles used for the reconstruction of the morphological throws. Spatial distribution of (b) morphological throw and (c) 2018 coseismic vertical offset. Note that the vertical axes are not in scale.

Moreover, we note that: i) the new trace clearly approaches the buried fault MCF that thus can be considered as the northernmost segment of the whole fault system (FF+MCF+ACF, cfr.

Figure 1b); ii) the continuity of the fault system (FF+MCF) represents a structural weakness that favoured, in the past, the dyke intrusion responsible for the eruption of Mt. Ilice [see examples in *Tibaldi*, 1995; *Corazzato e Tibaldi*, 2006; *Riedel et al.*, 2006; *Azzaro et al.*, 2012]; iii) the Mt. Ilice scoria cone testifies to the tectonic discontinuity between the FF and MCF, indeed representing the northern boundary of FF.

Moving southward, the boundary of the FF with the ACF can be identified where the long-term throw minimum ranges from 4.7 to 10.2 m (x = 7500 m in Figure 13b). The profile shape of the ACF scarp is symmetrical and characterized by a much larger height with a central peak of 79.6 ± 5.1 m tapering at both ends. In this case, the scarp morphology is well-preserved (see exposed faults in *Azzaro et al.*, 2012), being strongly controlled by the ancient lithologies and structures of the underlying bedrock mostly consisting of old lavas (S. Alfio Synthem, about 110-120 kyr, see Figure 3).

Unfortunately, it is not possible to calculate a reliable slip-rate by means of the age of the displaced lava flows (Figure 3) and the height of the fault scarp (Figure 13b). In fact, the resulting values are extremely variable along the strike, even at very short distances, depending on the lava flows that cross (or mantle) the fault scarp without resetting its height to zero. This provides an overestimation of the real throw rate, since the morphologic throw was built in a former period, older than the overlying geological formations.

4.3 Fault model and SHA implications

Lastly, we summarize some of the aforementioned points to propose a conceptual model with implications on the seismogenic potential of the FF. To this end, in the scheme of Figure 14a we illustrate the geometrical relationships among the FF, ACF and MCF, along with their seismotectonic behaviour. Taking into account the characteristics of the coseismic surface faulting observed during the past earthquakes, we note that: i) the seismogenic sector (in grey) was entirely ruptured during the 1894 and 2018 earthquakes, ii) no earthquake ruptures extended into the creeping section to the south (in blue).

As for the first point, we observe that the overall extent of the seismogenic segment of the FF, ca. 7.5 km, is equal to the 2018 rupture length and of the same order of magnitude of the theoretical length calculated by the magnitude-size scaling relationship (MSR) specific for the Mt. Etna area [*Azzaro et al.*, 2017]. The empirical scaling relationship between magnitude and rupture

length (Figure 14b) shows that 2018-like M_W 5.0 events produce 6 km-long coseismic ruptures. The 7.5 km-long rupture observed in the 2018 falls into the epistemic uncertainty associated with the MSR calibration, deriving both from errors in determining the magnitude of historical earthquakes [*Azzaro et al.,* 2011] and from a frequent underestimation of the historical rupture lengths (geological surveys were not as detailed as today and the focus was on the more impressive field features).

The transtensional FF releasing bend constitutes a geometrical irregularity that is unable to play the role of permanent segment boundary, as demonstrated by the 2018 event. However, it could have controlled: 1) initiation of the 2018 earthquake rupture/location of the mainshock hypocenter; 2) slip distribution; 3) possible early rupture termination to the south. In fact, the releasing bend determines a strong reduction of the σ_n and resultant decreasing of frictional resistance (i.e. unclamping). This could have favoured the propagation of the 2018 coseismic rupture on the southern section of the FF, promoting the locations of slip maxima ahead of the bend, as suggested by theoretical modeling [e.g. *Sibson* 1986; *Harris and Day,* 1993; *Kato et al.,* 1999; *Kase and Day,* 2006]. The coseismic rupture front of the 2018 mainshock terminated nearly 2.5 km beyond the N335° transtensional releasing bend of the FF, which strikes at 25° with respect to the main fault trace in the northern section (N310°). *Kas and Day* [2006] suggest that bends >20° can cause large excess stress and negative stress drop beyond the bend, which in turn should stop the rupture. On the other hand, according to *Barka and Kandinsky-Cade* [1988], fault bends >30° represent geometrical discontinuities that hamper propagation of rupture on strike-slip faults. In our opinion, it is likely that the 2018 rupture along the FF ripped through a geometrical barrier. Concerning the implications in terms of the source's geological model, the mainshock hypocenter is located near the transtensional releasing bend, at the southern edge of the northern section of the FF, where larger σ_n could provide more suitable mechanical conditions to originate asperities (cfr. Figure 12). This observation agrees with those of *Kadinsky-Cade and Barka* [1989] for most similar settings worldwide. As a whole, the location of mainshock and slip distribution along the transtensional bend suggest a southward 2018 rupture directivity.

Regarding the second point, this evidence is strictly related to the role played by a barrier in decoupling the FF segment from the ACF one, as already observed for other faults of Mt. Etna area [*Azzaro et al.,* 2020]. The pattern of the long-term morphological throw of the FF shown in Figure 13b clearly mimics the along-strike distribution of the coseismic mean vertical

displacement measured in the field (cfr. Figure 13c). This finding proves that the cumulative, long-term process of fault growth is the result of repeating individual rupture episodes due to major earthquakes like the 1894 and 2018 ones, in combination with more frequent smaller events, which suggest a Uniform Slip Model of displacement for the FF [*sensu Sieh*, 1981]. Note also that the geometrical boundary separating the two sections of the FF near Pennisi, hampers minor ruptures from propagating northwards, i.e. they do not rip through the fault bend.

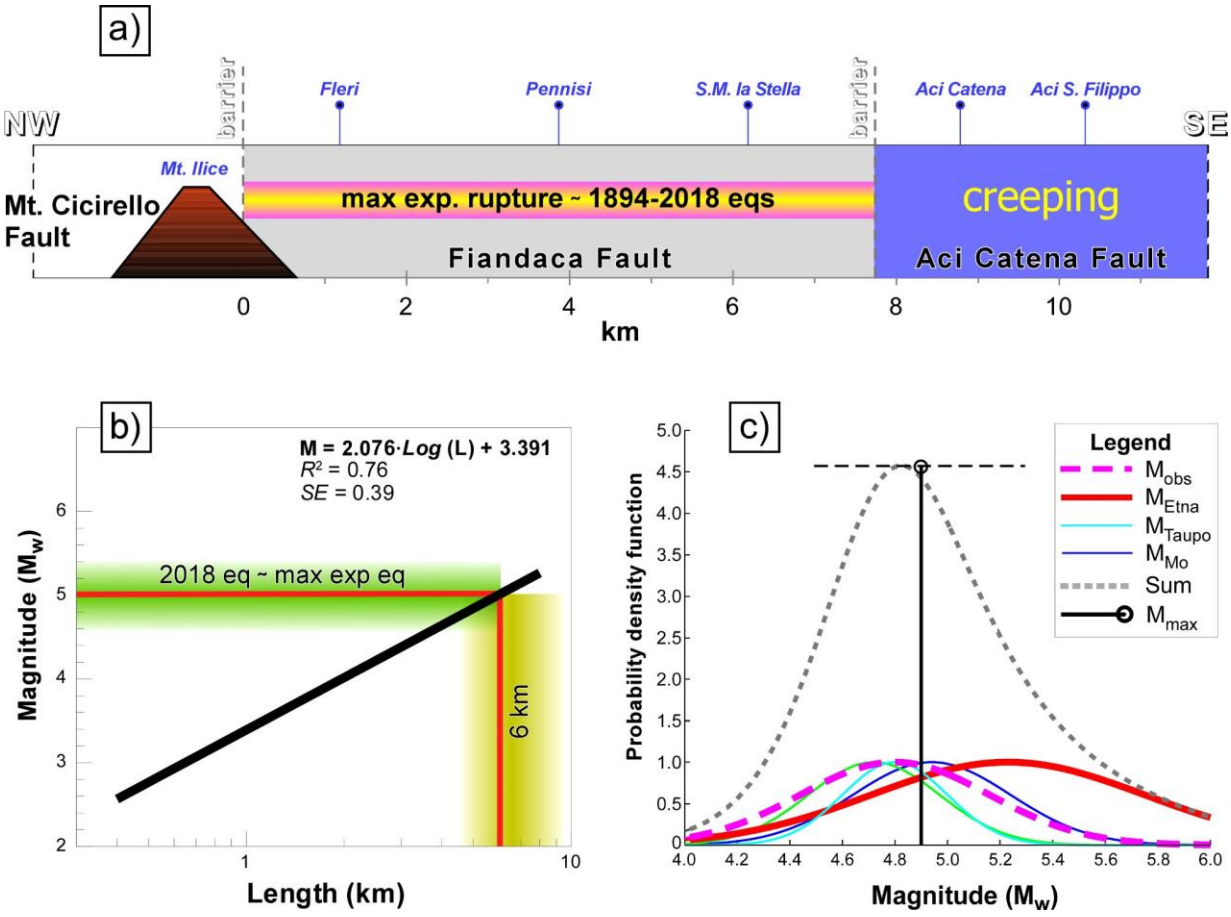

Figure 14. Seismogenic potential of the FF defined through fault-based seismic hazard assessment [for details see *Azzaro et al., 2017*]. (a) Conceptual model of behaviour of the Fiandaca fault system. The seismogenic segment (in grey) hosts the maximum observed earthquakes; the extension of the maximum historical coseismic surface faulting is also reported. (b) Earthquake scaling relationship between magnitude vs. rupture length for the Etna volcano-tectonic events. The theoretical value of fault length for a M_W 5.0 (2018 eq) with the associated uncertainty is also shown. (c) Maximum expected magnitude (M_{max}) estimated for the FF. Abbreviations: M_{obs}, maximum observed magnitude; M_{etna} - M_{Taupo}, magnitude from earthquake scaling relationships for the Etna and Taupo (New Zealand) volcanic regions; M_{Mo}, scalar seismic moment magnitude; Sum, summation of the probability density functions; M_{max}, central value of the Gaussian fit and associated standard deviation (horizontal dashed line).

In conclusion, the above results converge to define the seismogenic potential of the fault, here expressed in terms of maximum magnitude (M_{max}) expected for the FF. In Figure 14c, we recall the results obtained by *Azzaro et al.* [2017] through the probabilistic approach of the FiSH code [*Pace et al.*, 2016]. In short, M_{max} is the result of the summation (dashed curve) of the probability density functions related to the estimate of the maximum possible magnitude by means of different MSRs, aspect ratio relationships, seismic moment conversion and maximum observed magnitude. The value of M_{max} obtained for the FF is 4.9, very consistent with the M_W 5.0 instrumentally derived.

5 Conclusions

Although coseismic surface faulting is a well-known and documented feature at Mt. Etna volcano, this is the first time that a complex and extended earthquake rupture like the 2018 event has been mapped in fine detail. The geological survey carried out along the Fiandaca fault has allowed collecting a large amount of measurements and observations that shed light on the mechanism of faulting of the M_w 5.0 2018 event, as well as on the morphotectonic process of fault growth in the long-term.

In general, this study confirms and corroborates the following seismotectonic features: i) the Fiandaca fault is a segment characterised by stick-slip (i.e. seismogenic) behaviour that connects to the adjacent Aci Catena fault segment, conversely characterized by stable sliding behaviour; ii) the two fault segments are separated by a persistent barrier that hampers earthquake ruptures from propagating southwards; iii) kinematics revealed by the past earthquake ruptures is almost constant along the strike, while offset and extension depend on the magnitude of the events.

In detail, the main findings emerging from the analysis of our field data indicate that:

• the 2018 earthquake ruptured the whole locked segment of the Fiandaca fault for a length of 7.5 km, with the displacement mostly confined along the main fault trace and few off-fault secondary ruptures;

• the principal displacement zone of the 2018 rupture runs along the two sections of the Fiandaca fault, changing strike from NW-SE to NNW-SSE and crossing the bend, which appears as a “violated” geometrical discontinuity;

• the pattern of the 2018 surface rupture is characterised by scale-invariant overlapping systems of structures, organised in a hierarchical way from individual *en-échelon* ruptures

(defining the single displacement zones) to groups of structures, whose envelope defines the principal surface rupture zone, i.e. the surface expression of the seismogenic slip plane;

• the 2018 surface pattern varies along the strike due to the bending and consequent increasing oblique divergence between the fault blocks, showing a prevailing right-lateral kinematics in the northern section and a dextral oblique slip (max 33 cm) in the southern one, with the dip-slip component increasing southward (max 50 cm); this finding suggests a quasi-rigid behaviour of the crustal fault blocks;

• the increasing oblique divergence of the two fault blocks determined an unclamping that favoured the propagation of the 2018 coseismic rupture on the southern section of the Fiandaca fault. For the same reason, its northern section is characterized by mechanical conditions that are more suitable to host the asperity and hence the mainshock location;

• the along-strike distribution of the coseismic vertical displacement mimics the pattern of the long-term morphological throw of the Fiandaca fault, i.e. we highlighted the basic process of the fault growth;

• the trace of the hidden section of the Fiandaca fault appears to be connected with the pyroclastic cone of Mt. Ilice; the continuity with the nearby Mt. Cicirello fault is evident, revealing a fault system (i.e. a volcano's structural weakness zone) more extended than previously known.

• the 2018 event, together with the 1894 one, represents the major earthquake of the Fiandaca fault while other minor events repeatedly ruptured patches of the same structure as for the Uniform Slip Model [*Sieh*, 1981];

• the rupture length of the 2018 event is in the range of values expected from the magnitude-size scaling relationship for a M_w 5.0 earthquake at Etna; this magnitude value corresponds to the maximum potential earthquake calculated independently by a probabilistic geological approach.

The interpretation of the 2018 earthquake rupture in the framework of the well-known geological setting and seismic history of the Fiandaca fault, confirms that Etna represents a perfect natural laboratory also for active tectonics, where field observations are essential to constrain the behaviour of a seismogenic structure as well as to improve fault-based seismic hazard assessment.

Acknowledgments

We wish to thank all those who were directly affected by the earthquake and who kindly provided information and access to their properties, and particularly N. D'Alescio (owner of the site in Figure 5a). The field activities during the 2018 Etna emergency were funded by the Italian Civil Protection Department; the regional Civil Protection Department of Sicily is acknowledged for the support in the logistics of the survey. No potential conflict of interest was reported by the authors.

Data Availability Statement

All field data used in this study are taken from Civico et al., 2019 (doi: 10.1080/17445647.2019.1683476) and Villani et al., 2020 (doi: https://doi.org/10.1038/s41597-020-0383-0), and their supplementary materials.

References

Acocella, V., and M. Neri (2005), Structural features of an active strike-slip fault on the sliding flank of Mt. Etna (Italy). J. Struct. Geology 27(2), 343-355.

Aloisi, M., M. Mattia, C. Monaco, and F. Pulvirenti (2011), Magma, faults, and gravitational loading at Mount Etna: the 2002–2003 eruptive period, J. Geophys. Res., 116, B05203, doi:10.1029/2010JB007909.

Alparone, S., G. Barberi, E. Giampiccolo, V. Maiolino, A. Mostaccio, C. Musumeci, A. Scaltrito, L. Scarfì, T. Tuvè, and A. Ursino (2020), Seismological constraints on the Mt. Etna (Italy) 2018 flank eruption and implications in the volcano flanks dynamics, Terra Nova J., 32(5), https://doi.org/10.1111/ter.12463.

Azzaro, R. (1999), Earthquake surface faulting at Mount Etna volcano (Sicily) and implications for active tectonics, J. Geodyn., 28, 193-213.

Azzaro, R. (2004), Seismicity and active tectonics in the Etna region: constraints for a seismotectonic model. In: Bonaccorso, A., S. Calvari, M. Coltelli, C. Del Negro, and S. Falsaperla (Eds.), Mt. Etna: Volcano laboratory, Am. Geoph. Union, 205-220, doi:10.1029/GM143.

Azzaro, R., S. D'Amico, and T. Tuvè (2011), Estimating the magnitude of historical earthquakes from macroseismic intensity data: new relationships for the volcanic region of Mount Etna (Italy), Seism. Res. Lett., 82 (4), 520-531.

709 Azzaro, R., S. Branca, K. Gwinner and M. Coltelli (2012), The volcano-tectonic map of Etna
710 volcano, 1:100.000 scale: morphotectonic analysis from high-resolution DEM integrated with
711 geologic, active faulting and seismotectonic data, It. J. Geosciences, 131(1), 153-170.
712 Azzaro, R., A. Bonforte, S. Branca, and F. Gugliemino (2013a), Geometry and kinematics of the
713 fault systems controlling the unstable flank of Etna volcano (Sicily), J. Volcanol. Geoth. Res.,
714 251, 5-15, doi:10.1016/j.jvolgeores.2012.10.001.
715 Azzaro, R., S. D'Amico, L. Peruzza, and T. Tuvè (2013b), Probabilistic seismic hazard at Mt. Etna
716 (Italy): the contribution of local fault activity in mid-term assessment, J. Volcanol. Geotherm.
717 Res., 251, 158–169.
718 Azzaro, R., G. Barberi, S. D'Amico, B. Pace, L. Peruzza, and T. Tuvè (2017), When probabilistic
719 seismic hazard climbs volcanoes: the Mt. Etna case, Italy – Part 1: Model components for
720 sources parameterization, Nat. Hazards Earth Syst. Sci., 17, 1981–1998,
721 https://doi.org/10.5194/nhess-17-1981-2017.
722 Azzaro, R., and S. D'Amico (2019), Catalogo Macrosismico dei Terremoti Etnei (CMTE) (1633-
723 2018). Istituto Nazionale di Geofisica e Vulcanologia, https://doi.org/10.13127/cmte.
724 Azzaro, R., A. Bonforte, S. D'Amico, F. Guglielmino, and L. Scarfì (2020), Stick-slip vs. stable
725 sliding fault behaviour: a case-study using a multidisciplinary approach in the volcanic region
726 of Mt. Etna (Italy), Tectonophysics, 790, 228554, https://doi.org/10.1016/j.tecto.2020.228554
727 Baize, S., F. Nurminen, A. Sarmiento, T. Dawson, M. Takao, O. Scotti, T. Azuma, P. Boncio, J.
728 Champenois, F.R. Cinti, R. Civico, C. Costa, L. Guerrieri, E. Marti, J. McCalpin, K. Okumura,
729 and P. Villamor (2019), A worldwide and unified database of Surface Ruptures (SURE) for
730 Fault Displacement Hazard Analyses, Seismol. Res. Lett., doi: 10.1785/0220190144.
731 Barka, A. A., and K. Kadinsky-Cade (1988), Strike-slip fault geometry in Turkey and its influence
732 on earthquake activity, Tectonics, 7(3), 663-684.
733 Barreca, G., A. Bonforte, and M. Neri (2012), A GIS tool for integrated hazard evaluation on the
734 faults of Mt. Etna (Sicily), J. Volcanol. Geotherm. Res., 251, 170-186, doi:
735 10.1016/j.jvolgeores.2012.08.013.
736 Bonforte, A., F. Guglielmino, M. Coltelli, A. Ferretti, and G. Puglisi (2011), Structural assessment
737 of Mount Etna volcano from Permanent Scatterers analysis, Geochem. Geophys. Geosyst., 12,
738 doi:10.1029/2010GC003213.

739 Bonforte, A., F. Gugliemino, and G. Puglisi (2019), Large dyke intrusion and small eruption: the
740 December 24, 2018 Mt. Etna eruption imaged by Sentinel-1 data. Terra Nova, 31, 405-412,
741 doi: 10.1111/ter.12403.
742 Branca, S., M. Coltelli, G. Groppelli, and F. Lentini (2011a), Geological map of Etna volcano,
743 1:50,000 scale, It. J. Geosciences, 130(3), 265–291. doi:10.3301/IJG.2011.15
744 Branca, S., M. Coltelli, and G. Groppelli (2011), Geological evolution of a complex basaltic
745 stratovolcano: Mount Etna, Italy, It. J. Geosci., 130(3), 306-317, doi: 10.3301/IJG.2011.13
746 Branca, S., and T. Abate (2019), Current knowledge of Etna's flank eruptions (Italy) occurring
747 over the past 2500 years. From the iconographies of the XVII century to modern geological
748 cartography, J. Volcanol. Geotherm. Res., 385, 159-178. DOI:
749 10.1016/j.jvolgeores.2017.11.004
750 Cannavò, F., S. Gambino, B. Puglisi, and R. Velardita (2016), Modeling ground deformation
751 associated with the destructive earthquakes occurring on Mt. Etna's southeastern flank in
752 1984, Nat. Hazards Earth Syst. Sci., 16, 2443–2453, doi:10.5194/nhess-16-2443-2016.
753 Catalano, S., A. Bonforte, F. Guglielmino, G. Romagnoli, C. Tarsia, and G. Tortorici (2013), The
754 influence of erosional processes on the visibility of Permanent Scatterers Features from SAR
755 remote sensing on Mount Etna (E Sicily), Geomorphology, 198, 128–137,
756 http://dx.doi.org/10.1016/j.geomorph.2013.05.020.
757 Civico, R., S. Pucci, R. Nappi, R. Azzaro, F. Villani, D. Pantosti, F.R. Cinti, L. Pizzimenti, S.
758 Branca, C.A. Brunori, M. Caciagli, M. Cantarero, L. Cucci, S, D'Amico, E. De Beni, P.M. De
759 Martini, M.T. Mariucci, P. Montone, R. Nave, T. Ricci, V. Sapia, A. Smedile, G. Tarabusi, R.
760 Vallone, and A. Venuti (2019), Surface ruptures following the 26 December 2018, Mw 4.9,
761 Mt. Etna earthquake, Sicily (Italy), Journal of Maps, 15(2), 831-837, doi:
762 10.1080/17445647.2019.1683476.
763 Corazzato, C., and A. Tibaldi (2006), Fracture control on type, morphology and distribution of
764 parasitic volcanic cones: an example from Mt. Etna, Italy, J. Volcan. Geotherm. Res., 158,
765 177-194.
766 Cucci, L., S. D'Amico, P.M. De Martini, R. Nave, L. Pizzimenti, R. Azzaro, S. Branca, C.A.
767 Brunori, M. Caciagli, M. Cantarero, F.R. Cinti, R. Civico, E. De Beni, M.T. Mariucci, A.
768 Messina, P. Montone, R. Nappi, D. Pantosti, S. Pucci, T. Ricci, A. Smedile, V. Sapia, G.
769 Tarabusi, R. Vallone, A. Venuti, and F. Villani (2019), Photographic collection of the

770 coseismic geological effects originated by the 26th December Etna (Sicily) earthquake,
771 Miscellanea INGV, 48, 1-76, https://doi.org/10.13127/misc/48.
772 De Novellis, V., S. Atzori, C. De Luca, M. Manzo, E. Valerio, M. Bonano, C. Cardaci, R. Castaldo,
773 D. Di Bucci, M. Manunta, G. Onorato, S. Pepe, G. Solaro, P. Tizzani, I. Zinno, M. Neri, R.
774 Lanari, and F. Casu (2019), DInSAR analysis and analytical modelling of Mt. Etna
775 displacements: the December 2018 volcano-tectonic crisis, Geoph. Res. Lett., 46, 5817–5827,
776 doi: 10.1029/2019GL082467.
777 De Paola, N., R.E. Holdsworth, and K.J.W. McCaffrey (2005), The influence of lithology and pre-
778 existing structures on reservoir-scale faulting patterns in transtensional rift zones, J. Geol.
779 Soc., 162(3), 471-480.
780 Gwinner, K., M. Coltelli, J. Flohrer, R. Jaumann, K.D. Matz, M. Marsella, T. Roatsch, F. Scholten,
781 and F. Trauthan (2006), The HRSC-AX Mt. Etna project: high-resolution orthoimages and 1
782 m DEM at regional scale, Int. Arch. Phot. Rem. Sens. XXXVI (Part 1),
783 http://isprs.free.fr/documents/Papers/T05-23.pdf.
784 Harris, R. A., and S. M. Day (1993), Dynamics of fault interaction: parallel strike-slip faults, J.
785 Geoph. Res.: Solid Earth, 98(B3), 4461-4472.
786 Johnson, A.M., R.W. Fleming, and K.M. Cruikshank (1994), Shear zones formed along long,
787 straight traces of fault zones during the 28 June 1992 Landers, California, earthquake. Bull.
788 Seism. Soc. Am., 84 (3), 499-510.
789 Kadinsky-Cade, K., and A. A. Barka (1989), Effects of restraining bends on the rupture of strike-
790 slip earthquakes. Fault segmentation and controls of rupture initiation and termination, US
791 Geol. Surv. Open File Rep, 89(315), 181-192.
792 Kase, Y., and S. M. Day (2006), Spontaneous rupture processes on a bending fault, Geoph. Res.
793 Let., 33 (10).
794 Kato, N., T. Satoh, X. Lei, K. Yamamoto, and T. Hirasawa (1999), Effect of fault bend on the
795 rupture propagation process of stick-slip, Tectonophysics, 310(1-4), 81-99.
796 Lazarte, C.A., J.D. Bray, A.M. Johnson, and R.E. Lemmer (1994), Surface breakage of the 1992
797 Landers earthquake and its effects on structures, Bull. Seism. Soc. Am., 84(3), 547-561.
798 Lentini, F., Carbone, S., and P. Guarnieri (2006), Collisional and post-collisional tectonics of the
799 Apenninic-Maghrebian orogen (southern Italy), In Dilek Y. and Pavlides (eds.),

Postcollisional Tectonics and Magmatism in the Mediterranean Region and Asia, Geol. Soc. Am., Special paper, 409, 57-81.

Monaco, C., G. Barreca, D. Bella, F. Brighenti, V. Bruno, F. Carnemolla, G. De Guidi, M. Mattia, M. Menichetti, M. Roccheggiani, L. Scarfì (2021), The seismogenic source of the 2018 December 26th earthquake (Mt. Etna, Italy): a shear zone in the unstable eastern flank of the volcano, J. Geodyn., 143, https://doi.org/10.1016/j.jog.2020.101807.

Pucci, S., N. Palyvos, C. Zabci, D. Pantosti, and M. Barchi (2006), Coseismic ruptures and tectonic landforms along the Düzce segment of the North Anatolian Fault Zone (Ms 7.1, November 1999), J. Geoph. Res.: Solid Earth, 111(B6).

QUEST Working Group (2019), Il terremoto etneo del 26 dicembre 2018, M_w4.9: rilievo degli effetti macrosismici, Report INGV n. 1, 2019/02/06, pp. 9, doi: 10.5281/zenodo.2558168. http://www.questingv.it/index.php/rilievi-macrosismici/36-etna-26-12-2018-mw-4-9.

Riedel, C., G. G. J. Ernst, and M. Riley (2003), Controls on the growth and geometry of pyroclastic constructs, J. Volcanol. Geotherm. Res. 127, 121–152.

Romagnoli, G., F. Pavano, G. Tortorici, and S. Catalano (2021), The 2018 Mount Etna earthquake (Mw 4.9): depicting a natural model of a composite fault system from coseismic surface breaks, Tectonics, 40, e2020TC006286, https://doi.org/10.1029/2020TC006286

Rovida, A., M. Locati, R. Camassi, B. Lolli, P. Gasperini, and A. Antonucci (eds) (2021), Italian Parametric Earthquake Catalogue (CPTI15), version 3.0, Istituto Nazionale di Geofisica e Vulcanologia (INGV). https://doi.org/10.13127/CPTI/CPTI15.3

Ruch, J., S. Pepe, F. Casu, G. Solaro, A. Pepe, V. Acocella, M. Neri, and E. Sansosti (2013), Seismo-tectonic behavior of the Pernicana Fault System (Mt. Etna): a gauge for volcano flank instability?, J. Geoph. Res., Solid Earth, 118, 4398–4409, doi:10.1002/jgrb.50281.

Sibson, R.H. (1986), Rupture interaction with fault jogs, In: Das, S., J. Boatwright,, C.H. Scholz (Eds.), Earthquake Source Mechanics, Am. Geoph. Union, Washington, D.C., 157–167.

Sieh, K. E. (1981), A review of geological evidence for recurrence times of large earthquakes. In: *Earthquake Prediction-An International Review*, Maurice Ewing Set., vol. 4, D. W. Simpson and P. G. Richards (Eds.), pp. 181-207, Washington, DC: American Geophysical Union.

Sieh, K., L. Jones, E. Hauksson, K. Hudnut, D. Eberhart-Phillips, T. Heaton, S. Hough, K. Hutton, H. Kanamori, A. Lilje, S. Lindvall, S.F. McGill, J. Mori, C. Rubin, J.A. Spotila, J. Stock, H.K.

Thio, J. Treiman, B. Wernicke, and J. Zachariasen (1993), Near-field investigations of the Landers earthquake sequence, April to July 1992, Science, 260(5105), 171-176.

Solaro, G., V. Acocella, S. Pepe, J. Ruch, M. Neri, and E. Sansosti (2010), Anatomy of an unstable volcano from InSAR: multiple processes affecting flank instability at Mt. Etna, 1994–2008, J. Geophys. Res., Solid Earth, 115(B10), doi: 10.1029/2009JB000820.

Tanguy, J. C., M. Condomines, S. Branca, S. La Delfa, and M. Coltelli (2012), New archeomagnetic and 226Ra-230Th dating of recent lavas for the Geological map of Etna volcano, Ital. J. Geosci., 131(2), 241-257. doi: 10.3301/IJG.2012.01

Tchalenko, J. S., and N.N. Ambraseys (1970), Structural analysis of the Dasht-e Bayaz (Iran) earthquake fractures, Geol. Soc. Am. Bull., 81(1), 41-60.

Tchalenko, J. S., and M. Berberian (1975), Dasht-e Bayaz fault, Iran: earthquake and earlier related structures in bed rock, Geol. Soc. Am. Bull., 86(5), 703-709.

Tibaldi, A. (1995), Morphology of pyroclastic cones and tectonics, J. Geophys. Res., Solid Earth, 110(B12), 24521-24535, https://doi.org/10.1029/95JB02250.

Tortorici, G., F. Pavano, G. Romagnoli, and S. Catalano (2021), The effect of recent resurfacing in volcanic areas on the distribution of co-seismic ground deformation due to strike-slip earthquakes: new insights from the 12/26/2018 seismic event at Mt. Etna, J. Struct. Geol., 145, https://doi.org/10.1016/j.jsg.2021.104308.

Urlaub, M., F. Petersen, F. Gross, A. Bonforte, G. Puglisi, F. Guglielmino, S. Krastel, D. Lange, and H. Kopp (2018), Gravitational collapse of Mount Etna's southeastern flank, Sci. Advances, 4(10), eaat9700 doi: 10.1126/sciadv.aat9700.

Villani, F., S. Pucci, R. Azzaro, R. Civico, F. Cinti, L. Pizzimenti, G. Tarabusi, S. Branca, C. A. Brunori, M. Caciagli, M.Cantarero, L. Cucci, S. D'Amico, E. De Beni, P. M. De Martini, M. T. Mariucci, A. Messina, P. Montone, R. Nappi, R. Nave, D. Pantosti, T. Ricci, V. Sapia, A. Smedile, R. Vallone, and A. Venuti (2020), Surface ruptures database related to the 26 December 2018, Mw 4.9, Mt. Etna earthquake, southern Italy, Sci. Data, 7(42), 1-9, Doi: https://doi.org/10.1038/s41597-020-0383-0.

Wilcox, R. E., T. T. Harding, and D. R. Seely (1973), Basic wrench tectonics, American Association of Petroleum Geologists, Bulletin, 57, 74-95.

Withjack, M. O., and W. R. Jamison (1986), Deformation produced by oblique rifting, Tectonophysics, 126(2-4), 99-124.

Yeats, R. S., K. Sieh, and C. R. Allen (1997), The geology of earthquakes, Oxford University Press, 568 pp.